Nanoscale c8nr08781d

We have presented the Graphical Abstract text and image for your article below. This brief summary of your work will appear in the contents pages of the issue in which your article appears.

1

A sequentially responsive and structure-transformable nanoparticle with a comprehensively improved 'CAPIR cascade' for an enhanced antitumor effect

Chenfeng Xu, Yu Sun, Yulin Yu, Mei Hu, Conglian Yang and Zhiping Zhang*

A sequentially responsive and structure-transformable nanoparticle was designed for comprehensively improving circulation, accumulation, penetration, internalization and release in drug delivery.

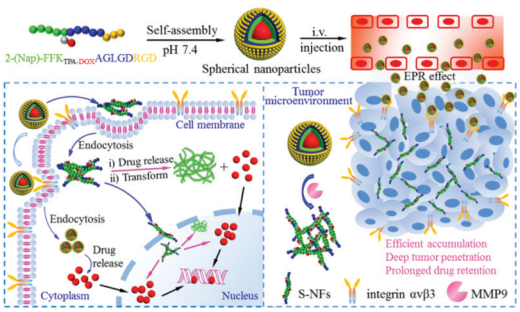

Please check this proof carefully. Our staff will not read it in detail after you have returned it.

Please send your corrections either as a copy of the proof PDF with electronic notes attached or as a list of corrections. **Do not edit the text within the PDF or send a revised manuscript** as we will not be able to apply your corrections. Corrections at this stage should be minor and not involve extensive changes.

Proof corrections must be returned as a single set of corrections, approved by all co-authors. No further corrections can be made after you have submitted your proof corrections as we will publish your article online as soon as possible after they are received.

Please ensure that:

- The spelling and format of all author names and affiliations are checked carefully. You can check how we have identified the authors' first and last names in the researcher information table on the next page. **Names will be indexed and cited as shown on the proof, so these must be correct.**
- Any funding bodies have been acknowledged appropriately and included both in the paper and in the funder information table on the next page.
- All of the editor's queries are answered.
- Any necessary attachments, such as updated images or ESI files, are provided.

Translation errors can occur during conversion to typesetting systems so you need to read the whole proof. In particular please check tables, equations, numerical data, figures and graphics, and references carefully.

Please return your **final** corrections, where possible within **48 hours** of receipt, by e-mail to: nanoscale@rsc.org. If you require more time, please notify us by email.

Funding information

Providing accurate funding information will enable us to help you comply with your funders' reporting mandates. Clear acknowledgement of funder support is an important consideration in funding evaluation and can increase your chances of securing funding in the future.

We work closely with Crossref to make your research discoverable through the Funding Data search tool (http://search.crossref.org/funding). Funding Data provides a reliable way to track the impact of the work that funders support. Accurate funder information will also help us (i) identify articles that are mandated to be deposited in **PubMed Central (PMC)** and deposit these on your behalf, and (ii) identify articles funded as part of the **CHORUS** initiative and display the Accepted Manuscript on our web site after an embargo period of 12 months.

Further information can be found on our webpage (http://rsc.li/funding-info).

What we do with funding information

We have combined the information you gave us on submission with the information in your acknowledgements. This will help ensure the funding information is as complete as possible and matches funders listed in the Crossref Funder Registry.

If a funding organisation you included in your acknowledgements or on submission of your article is not currently listed in the registry it will not appear in the table on this page. We can only deposit data if funders are already listed in the Crossref Funder Registry, but we will pass all funding information on to Crossref so that additional funders can be included in future.

Please check your funding information

The table below contains the information we will share with Crossref so that your article can be found *via* the Funding Data search tool. **Please check that the funder names and grant numbers in the table are correct and indicate if any changes are necessary to the Acknowledgements text.**

Funder name	Funder's main country of origin	Funder ID (for RSC use only)	Award/grant number
Q1 National Natural Science Foundation of China	China	501100001809	81673374 81373360

Researcher information

Please check that the researcher information in the table below is correct, including the spelling and formatting of all author names, and that the authors' first, middle and last names have been correctly identified. **Names will be indexed and cited as shown on the proof, so these must be correct.**

If any authors have ORCID or ResearcherID details that are not listed below, please provide these with your proof corrections. Please ensure that the ORCID and ResearcherID details listed below have been assigned to the correct author. Authors should have their own unique ORCID iD and should not use another researcher's, as errors will delay publication.

Please also update your account on our online manuscript submission system to add your ORCID details, which will then be automatically included in all future submissions. See here for step-by-step instructions and more information on author identifiers.

First (given) and middle name(s)	Last (family) name(s)	ResearcherID	ORCID iD
Chenfeng	Xu		
Yu	Sun		
Yulin	Yu		
Mei	Hu		
Conglian	Yang		
Zhiping	Zhang		0000-0001-9975-4862

Queries for the attention of the authors

Journal: **Nanoscale** Paper: **c8nr08781d**

Title: **A sequentially responsive and structure-transformable nanoparticle with a comprehensively improved 'CAPIR cascade' for an enhanced antitumor effect**

For your information: You can cite this article before you receive notification of the page numbers by using the following format: (authors), Nanoscale, (year), DOI: 10.1039/c8nr08781d.

Editor's queries are marked like this Q1, Q2, and for your convenience line numbers are indicated like this 5, 10, 15, ...

Please ensure that all queries are answered when returning your proof corrections so that publication of your article is not delayed.

Query Reference	Query	Remarks
Q1	Funder details have been incorporated in the funder table using information provided in the article text. Please check that the funder information in the table is correct.	
Q2	Please confirm that the spelling and format of all author names is correct. Names will be indexed and cited as shown on the proof, so these must be correct. No late corrections can be made.	
Q3	Do you wish to add an e-mail address for the corresponding author? If so, please provide the relevant information.	
Q4	The sentence beginning "The result, unsurprisingly..." has been altered for clarity. Please check that the meaning is correct.	
Q5	The meaning of the phrase "has also to be confronted with" in the sentence beginning "In addition, traditional topical..." is not clear - please provide alternative text.	
Q6	The sentence beginning "Recently, peptides and their..." has been altered for clarity. Please check that the meaning is correct.	
Q7	The sentence beginning "It was permeable in the tumor..." has been altered for clarity. Please check that the meaning is correct.	
Q8	The meaning of the phrase "subsequent by a weak acid" in the sentence beginning "Chemical structure change of 2-(Nap)-FFK$_{TPA-DOX}$AGLDDRGD..." is not clear - please provide alternative text.	
Q9	The meaning of the word "performed" in the sentence beginning "The frozen sections were..." is not clear - please provide alternative text.	
Q10	The sentence beginning "The *in vivo* antitumor efficacy..." has been altered for clarity. Please check that the meaning is correct.	
Q11	In the sentence beginning "In parallel, the cytotoxicity..." should "four" be changed to "five"?	

Q12	The sentence beginning “The results indicated that the nanoparticles…” has been altered for clarity. Please check that the meaning is correct.	
Q13	Please indicate where ref. 51 should be cited in the text.	

Nanoscale

PAPER

A sequentially responsive and structure-transformable nanoparticle with a comprehensively improved 'CAPIR cascade' for an enhanced antitumor effect†

Cite this: DOI: 10.1039/c8nr08781d

Chenfeng Xu,[a] Yu Sun,[b] Yulin Yu,[a] Mei Hu,[a] Conglian Yang[a] and Zhiping Zhang *[a,c,d]

Received 31st October 2018,
Accepted 11th December 2018

DOI: 10.1039/c8nr08781d

rsc.li/nanoscale

An intravenously administered drug delivery system should undergo a five-step 'CAPIR' cascade (circulation, accumulation, penetration, internalization and release), and the maximal efficiency of each step is of great importance to obtain the improved final therapeutic benefits and overall survival rate. Here, a pH/matrix metalloproteinase-9 (MMP9) sequentially responsive and continuously structure-transformable nanoparticle assembled from a doxorubicin (DOX)-conjugated peptide was exploited for comprehensively improving the 'CAPIR cascade' and eventually enhancing the therapeutic efficacy. The chimeric peptide can self-assemble into spherical nanoparticles (RGD-sNPs) at pH 7.4 with a particle size of 45.7 ± 5.4 nm. By a combination of passive and active targeting mechanisms, RGD-sNPs achieved efficient accumulation at the tumor site (~15.1% ID g^{-1} within 24 h). Both *in vitro* and *in vivo* experiments revealed that RGD-sNPs can be transformed into rod-like nanoparticles (S-NFs) triggered by MMP9 that overexpressed in the tumor microenvironment, demonstrating remarkable advantages of deep tumor penetration, prolonged drug retention with ~3.7% ID g^{-1} at 96 h, and 2-fold enhanced internalization. Subsequently, S-NFs would respond to the intracellular weakly acidic stimuli to rapidly release DOX for induction of cytotoxicity and apoptosis. Meanwhile, the remaining peptide was further converted into long fibers (length >5 μm) with significant cytotoxicity, thereby exerting a synergistic antitumor effect. Thus RGD-sNPs displayed superior antitumor efficacy and extended the median survival period to 55 days. This provides a new horizon for the exploration of high-performance antitumor nanomedicines.

1. Introduction

Nanoparticle-based drug delivery systems (DDSs) for cancer chemotherapy have always been considered as particularly promising and are advancing rapidly.[1,2] However, the current clinical application of anticancer nanomedicines achieved no significantly enhanced therapeutic efficacy or only modest improvement in the overall survival rate of patients, in spite of certain advantages, including ameliorative pharmacokinetic properties and bioavailability, prolonged circulation time and reduced side effects.[3–6] For instance, Doxil®, a clinically applied pegylated liposomal doxorubicin (DOX), has shown an extended systemic circulation time of more than 30 h and considerable accumulation in the tumor region. Unfortunately, such improvements can only mitigate the dose-dependent adverse effects but fail to enhance the curative effect of DOX. It was further revealed that a large quantity of Doxil® was distributed around the periphery of blood vessels.[3,7] The result, unsurprisingly, is poor tumor penetration, let alone inefficient cellular uptake and slow intracellular drug release.[3,8,9] Thus, the rational design of cancer nanomedicines with more efficient therapeutic benefits is still an urgent demand.

It is generally accepted that the ultimate aim of drug delivery is to specifically transport the medicaments to target cells or organelles, and eventually exert their pharmacological activities as active drugs.[10] Admittedly, the localized DDSs which are directly implanted into the tumor tissue can indeed achieve high and persistent local drug concentration and decreased total dosage.[11] Nevertheless, the application of local carriers is strictly limited due to the difficulty of proper

[a]Tongji School of Pharmacy, Huazhong University of Science and Technology, Wuhan 430030, China
[b]Ningbo First Hospital, Ningbo 315010, China
[c]National Engineering Research Center for Nanomedicine, Huazhong University of Science and Technology, Wuhan 430030, China
[d]Hubei Engineering Research Centre for Novel Drug Delivery System, Huazhong University of Science and Technology, Wuhan 430030, China

†Electronic supplementary information (ESI) available. See DOI: 10.1039/c8nr08781d

implantation in the confined tumor region as well as increased operative trauma and medical risk.[12,13] In addition, traditional topical embedding administration has also to be confronted with the aforementioned conundrums including deep penetration, efficient cellular uptake and controlled drug release.[11] As previously reported, a typical intravenously administered DDS should undergo at least five successive steps: circulation in the bloodstream and accumulation in the tumor region, followed by penetration into the tumor tissue, internalization in the tumor cells and, ultimately, intracellular drug release, a 'CAPIR cascade' for short.[3,14,15] Obviously, it is of great importance to maximize the efficiency of each step for the improvement of final therapeutic benefits.

Recently, peptides and their associated DDS, such as peptide vaccination, nanoparticles, nanofibers, *etc.*, have experienced profound and rapid development. Among them, peptide–drug conjugates provided an attractive strategy for anticancer drug delivery because of the merits of high drug loading, intrinsic low toxicity, simplicity and chemical versatility.[16–20] To achieve the desired characteristics, many candidate peptides with different functions, including biological recognition, cell penetration and stimuli-responsive properties, can be cleverly selected for the exploration of peptide-based DDSs.[21–23] Moreover, tailor-made peptide-based prodrugs can self-assemble into unique nanostructures. Generally, nanoparticles with different structures or geometrical shapes display diverse functions and characteristics. Non-spherical (such as disc-like or rod-shaped) nanoparticles have been reported to show advantages of accelerated internalization and deep penetration over size-matched spheres, apparently due to the shortest diameter (the width of the disc or rod) of nanoparticles.[24–26] In addition, particles with large enough length (the longest dimension of the disc or rod), such as a nanofiber or nanogel (>1 μm), would exhibit a prolonged retention time in the tumor site and probably synergistic antitumor efficacy.[26,27] This kind of particle, unfortunately, would be readily cleared by the reticuloendothelial system (RES) and mononuclear macrophage system (MPS) after intravenous administration.[28] With the development of supramolecular chemistry, chimeric peptide-based structure-transformable and *in situ* self-assembled prodrug nanocarriers open a new avenue for the design of DDSs with a comprehensively improved 'CAPIR cascade'.[12,29–33]

Herein, we exploited a pH/matrix metalloproteinase-9 (MMP9) sequentially responsive and continuously structure-transformable nanoparticle assembled from a DOX-conjugated peptide, with advantages of tumor targeting delivery, prolonged drug retention, deep tissue penetration, accelerated internalization and rapid intracellular drug release, aiming at improving the final therapeutic efficacy and extending the overall survival rate (Scheme 1). The responsive peptide–DOX conjugate (2-(Nap)-FFK$_{TPA-DOX}$AGLDDRGD, compound **1**) and the control (2-(Nap)-FFK$_{TPA-DOX}$WGLWDRGD, compound **2**) were synthesized, purified and identified systematically. Arg-Gly-Asp (RGD) is popularly regarded as a targeting ligand that specifically recognizes the integrin αvβ3 receptor that is overexpressed on the surface of various cancer cells.[12,34] Ala-Gly-Leu-Asp-Asp (AGLDD) served as a MMP9 responsive linker, and 2-naphthylacetic acid-Phe-Phe-Lys (2-(Nap)-FFK) was inclined to assemble into stable fibrous structures *via* intermolecular hydrogen bonds.[18,30,35] DOX was coupled to a peptide skeleton *via* a pH-responsive hydrazone bond using 4-formylbenzoic acid (TPA) as a linker. Compounds **1** and **2** can both self-assemble into nanoparticles (RGD-sNPs and RGD-nNPs, respectively) in pH 7.4 phosphate buffer solution (PBS) with a spherical form, relatively small size (<50 nm) and slightly negative charge (∼−10 mV). These features are beneficial for the acquisition of long circulation in the blood and the avoidance of the formation of a protein corona.[36] Initially, RGD-sNPs efficiently extravasated and accumulated at the tumor site through a combination of an enhanced permeability and retention (EPR) effect and a RGD-mediated active targeting mechanism. Thereafter, MMP9, which has been proved to be highly expressed in the tumor stroma, will selectively cleave the AGLDD linker, leading to the structural transformation from spherical nanoparticles into rod-like nanoparticles (S-NFs, with an average diameter of 18 ± 1.6 nm and length of 225.7 ± 10.2 nm). It was permeable in the tumor microenvironment and easily internalized by cells as well as freely accessible to the nucleus, due to the very small diameter and suitable length. Finally, in the intracellular weakly acidic environment, active DOX would be quickly released for subsequent induction of cytotoxicity and apoptosis. The remaining peptide 2-(Nap)-FFK$_{TPA}$AG was gradually converted into long fibers (NapFFK-NFs, length >5 μm) with significant cytotoxicity, thereby exerting a synergistic antineoplastic effect by the caspase-3 apoptotic pathway and promiscuous interaction with microtubules as well as by a competitive combination with receptors on the surface of cells for the inhibition of downstream signal pathways.[18,27,30,33]

2. Experimental methods

2.1. Materials

2-(Nap)-FFKAGLDD-RGD (peptide 1, high resolution mass spectrometry (HRMS, ESI) *m*/*z*: ($[M + 2H]^{2+}$) calcd for $C_{67}H_{89}N_{15}O_{19}$, 705.25; found 705.38. Purity: 94.76%, Fig. S1 and S2†) and 2-(Nap)-FFKWGLWD-RGD (peptide 2, HRMS (ESI) *m*/*z*: ($[M + H]^{+}$) calcd for $C_{82}H_{99}N_{17}O_{17}$, 1594.8237; found 1594.8430. Purity: 93.37%, Fig. S3 and S4†) were obtained from Wuhan Bioyeargene Biosciences Co., Ltd. Doxorubicin hydrochloride (DOX·HCl) was purchased from Beijing Huafeng United Technology Co., China. Trifluoroacetic acid (TFA), 4% polyoxymethylene (PFA), 1-ethyl-3-(3-dimethylaminopropyl) carbodiimide hydrochloride (EDC·HCl), *N*-hydroxysuccinimide (NHS), TPA, anhydrous dimethylformamide (DMF) and d_6-dimethyl sulfoxide (d_6-DMSO) were purchased from Aladdin (Shanghai, China). Cy7.5-NHS was purchased from Xi'an Ruixi Biological Technology Co., Ltd. The MMP9 enzyme and 4-aminophenylmercuric acetate (APMA) were both purchased from Sino Biological Inc., Beijing. Phenylmethanesulfonyl fluoride

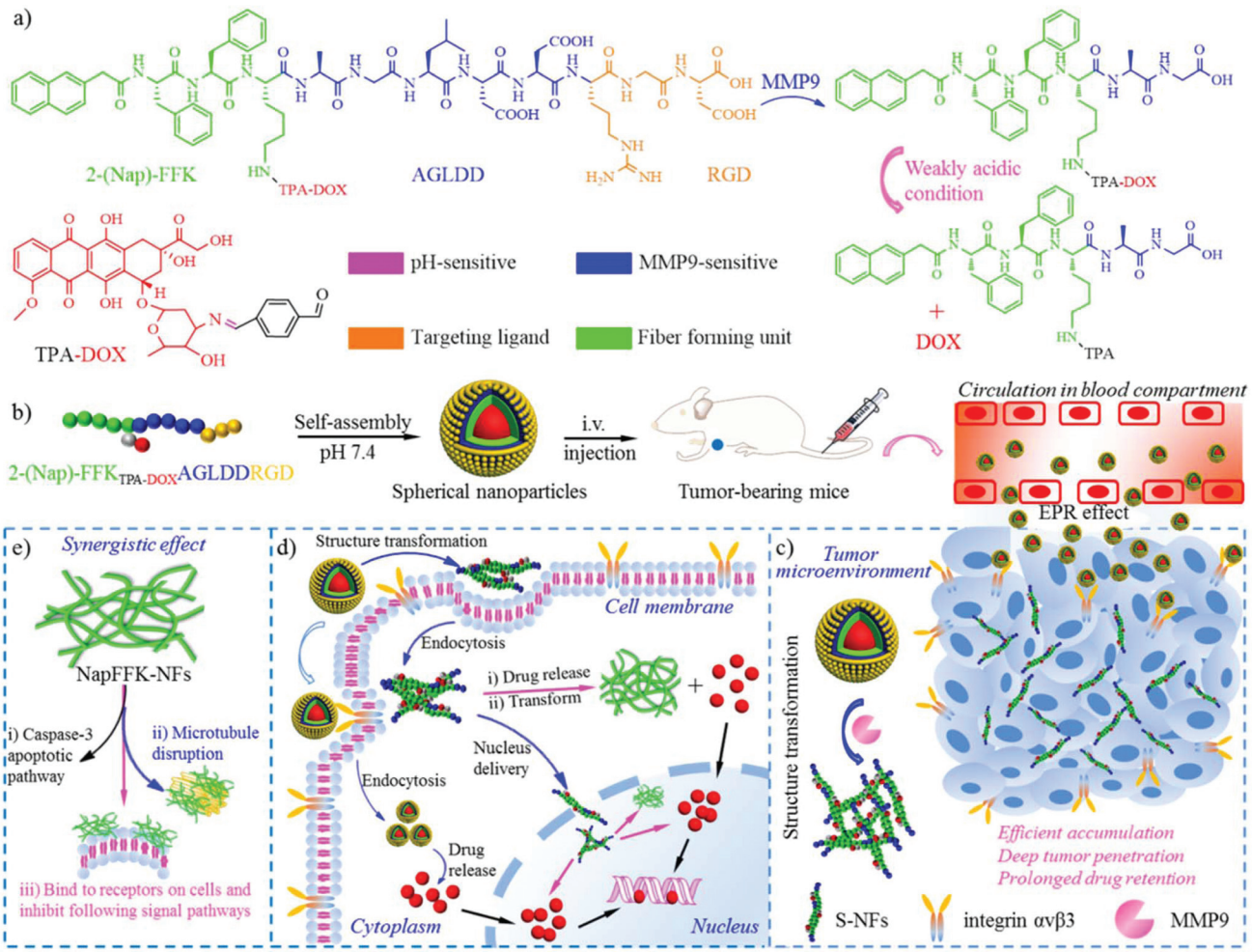

Scheme 1 Illustration of an improved 'CAPIR cascade' and an enhanced antitumor effect through a sequentially responsive and structure-transformable nanoparticle. (a) Chemical structure change of 2-(Nap)-FFK$_{TPA-DOX}$AGLDDRGD (compound **1**) triggered by MMP9 and subsequent by a weak acid (pH 5.5). (b) The self-assembly of compound **1** into spherical nanoparticles (RGD-sNPs), which were then intravenously administered into tumor-bearing mice and circulated for a long enough period of time in the blood compartment. (c) By a combination of the EPR effect and RGD-mediated active targeting mechanisms, RGD-sNPs can be efficiently accumulated in the tumor site. The gathered nanoparticles would be transformed into rod-like nanoparticles (S-NFs) with a suitable diameter and length due to the overexpressed MMP9 in the tumor microenvironment, resulting in deep tissue penetration, prolonged retention time and enhanced cellular uptake. (d) S-NFs were easily internalized by the cells, and DOX was rapidly released under weakly acidic conditions, for subsequent induction of cytotoxicity and apoptosis. The remaining 2-(Nap)-FFK$_{TPA}$-AG would be converted into long fibers (NapFFK-NFs, length >5 μm) with cytotoxicity. With the diameter of S-NFs smaller than the size of nucleopores, they have free access to the nuclear cavity, leading to high drug accumulation in the nucleus and inhibition of drug efflux. (e) The synergistic antitumor effect of NapFFK-NFs. It can cause apoptosis by the caspase-3 apoptotic pathway (i) and promiscuous interaction with microtubules (ii), and competitive combination with receptors on the surface of cells and subsequent inhibition of downstream signal pathways (iii).

(PMSF), 3-(4,5-dimethyl-thiazol-2-yl)-2,5-diphenyl tetrazolium bromide (MTT) and 4′,6-diamidino-2-phenylindole (DAPI) were purchased from Biosharp, South Korea. The RPMI 1640 medium, DMEM, penicillin–streptomycin, fetal bovine serum (FBS) and 0.25% trypsin without EDTA were purchased from Hyclone, GE Healthcare Life Sciences, USA. Alanine aminotransferase assay kits (ALT), aspartate aminotransferase assay kits (AST), creatinine assay kit (CRE), lactate dehydrogenase assay kit (LDH) and urea assay kit (BUN) were all purchased from Nanjing Jiancheng Bioengineering Institute, China. Other reagents were all obtained from Sinopharm Chemical Reagent Co. Ltd, Shanghai, China and were of analytical grade.

2.2. Cell culture

MCF-7/ADR and MCF-7 cells were obtained from Shanghai Institute of Medicine of Chinese Academy of Medical Sciences. Melanoma B16F10, Lewis lung carcinoma (LLC) and triple negative breast cancer (4T1) cells were purchased from the Chinese Academy of Sciences Cell Bank of China. HepG2 and H22 cells were kindly provided by Dr Guangya Xiang (Huazhong University of Science and Technology, HUST, China). The HepG2, B16F10, LLC and MCF-7 cells were all cultured in DMEM with 10% FBS, 100 U mL^{-1} penicillin and 100 μg mL^{-1} streptomycin, and maintained at 37 °C under a

humidified atmosphere of 90% in a 5% CO_2 incubator (Panasonic, Japan). The 4T1 cells were cultured in the complete RPMI 1640 medium under similar standard conditions. The MCF-7/ADR cells were cultured in the complete RPMI 1640 medium with the addition of 1 μg mL^{-1} DOX.

2.3. Animals

BALB/c mice (female 16–18 g) and Kunming mice (18–20 g) were both purchased from the Disease Control and Prevention Center of HUST. All animal experiments were approved by the Institutional Animal Care and Use Committee of HUST, and carried out according to the regulations of Chinese law and the local ethical committee.

2.4. Synthesis and characterization of conjugates

Compound **1** and compound **2** were both synthesized through a NHS ester activated carboxylic acid route (Fig. S5 and S6†).[37] TPA was firstly activated by NHS as previously reported (TPA-NHS), and then reacted with peptides 1 and 2 to obtain 2-(Nap)-FFK$_{TPA}$AGLDD-RGD and 2-(Nap)-FFK$_{TPA}$WDLWD-RGD, respectively.[38] Briefly, the peptide (1 eq.) and trimethylamine (1 eq.) were dissolved in DMSO in a vial, and then TPA-NHS (1.05 eq.) dissolved in DMSO was added dropwise into the peptide solution under stirring. After the reaction, the mixture was dialyzed against deionized water for 24 h, and subsequently lyophilized. Next, the TPA activated peptide was reacted with DOX (2 eq.) in DMF for 24 h at room temperature (RT). When the reaction was completed, the mixture was concentrated and the residue was redissolved in methanol. The crude product was purified by using a semi-preparative reverse-phase HPLC system (Agilent, 1100 series, USA) using an octadecylsilyl (ODS-A) 5 μm semi-preparative column (250 × 10 mm; Welch, Ultimate®). A gradient elution method (acetonitrile and water containing 0.1% TFA) was applied with a flow rate of 2 mL min^{-1}. The purity of compounds **1** and **2** was confirmed using analytical HPLC with a fluorescence detector at 470 nm/585 nm (ex/em). The analytical condition of HPLC is described as follows. A fluorescence detector was employed and the detection wavelength was set as 470 nm/585 nm (ex/em). A Kromasil ODS-SP C18 column (100-5-C18, 5 μm, 150 mm × 4.6 mm) was used and the column temperature was set at 30 °C. The mobile phase consisted of acetonitrile : water containing 0.1% TFA (25 : 75, v/v) and the flow rate was set as 1.0 mL min^{-1}.

The Cy7.5 labeled peptide was synthesized by a similar method. In brief, the peptide and Cy7.5-NHS (1.1 eq.) were dissolved in anhydrous DMF and reacted in the dark at 4 °C for 24 h. After the reaction was completed, the solvent was removed and the residue was precipitated with diethyl ether. The product was then collected by centrifugation, washed with diethyl ether and dried in a vacuum drying oven.

2.5. Preparation and characterization of nanoparticles

Nanoparticles self-assembled from compounds **1** and **2** (RGD-sNPs and RGD-nNPs, respectively) in a neutral environment (pH 7.4, 1 M PBS) were prepared by a modified rapid precipitation method.[39] 20 μL of the conjugate solution (DMSO, 50 mg mL^{-1}) was rapidly injected into 980 μL PBS under stirring (800 rpm) in the dark at RT, and the assembly occurred spontaneously. DMSO was removed by dialysis and the prepared nanoparticles were stored airtight and light-free at 4 °C. Cy7.5 labeled nanoparticles (Cy7.5-RGD-sNPs and Cy7.5-RGD-nNPs, respectively) were prepared by a similar method. These nanoparticles were characterized and determined by particle size and zeta potential using dynamic light scattering (DLS) along with transmission electron microscopy (TEM). To prepare TEM samples, 10 μL of freshly prepared nanoparticle suspension was dropped onto the surface of carbon-coated copper grids. The liquid was removed with filter paper after 15 min. The samples were stained with 1% phosphotungstic acid solution for 5 min, and then observed with a Tecnai G2 F20 TWIN TEM. The critical aggregation concentration (CAC) values were then evaluated by a pyrene probe method as reported.[30]

2.6. Verification of the structural transformation

To verify the MMP9 triggered structural transformation, freshly prepared nanoparticles (1 mg mL^{-1}, 1 mL) were dispersed and incubated at 37 °C with pH 6.8 PBS containing 50 ng mL^{-1} MMP9 and 1 μL of APMA. The reaction was terminated by the addition of the same volume of methanol after 2 h or 12 h of incubation, and then the reaction mixture was extracted with chloroform (3 mL × 2). The organic solvent was evaporated and the residue was redissolved in methanol for HPLC analysis as described above. At the predetermined time-point of 0.5, 1, 2, 4, 8 and 12 h, 10 μL of treated nanoparticle suspension was dropped onto the surface of carbon-coated copper grids for TEM analysis as well. To determine the selective cutting site, after 12 h of incubation, the reaction mixture was centrifuged at 12 000 rpm for 15 min, and washed with deionized water 2 times, followed by lyophilization for HRMS analysis. After 12 h of treatment, the precipitate was collected and dispersed with pH 5.5 PBS to estimate the pH-responsive structural transformation by similar assessment methods as mentioned above.

2.7. *In vitro* drug release

The *in vitro* DOX release was surveyed by a modified dialysis method. In brief, 2 mL of nano-preparation containing 1 mg of DOX was added into a dialysis bag (MWCO of 3.5 kDa), and then placed in 30 mL of the release medium (1 M PBS containing 0.1% Tween80) at pH 7.4, 6.8 and 5.5. The mixture was kept at 37 °C and shaken at 70–80 rpm. At designed time points, 5 mL of the solution was withdrawn and an equal volume of fresh buffer solution was added. DOX was extracted with chloroform, concentrated, redissolved in methanol, and measured by HPLC as described above.

2.8. *In vitro* cellular uptake

The cellular uptake of nanoparticles or nanofibers was estimated in HepG2 cells and 4T1 cells. Briefly, the cells were seeded in confocal microscopy dishes at a density of 5.0×10^4 cells per well and incubated overnight. Afterwards, free DOX,

RGD-nNPs, RGD-sNPs or pretreated RGD-sNPs (RGD-sNPs pretreated with MMP9 for 12 h) were separately added into the dish at a DOX concentration of 2 μg mL^{-1}, followed by 4 h or 24 h of incubation. The medium was then removed and the cells were washed with ice-cold PBS (1 M, pH 7.4) three times and subsequently fixed with 4% PFA for 15 min. Next, the cells were washed thrice with ice-cold PBS (1 M, pH 7.4) and stained with 20 μL of DAPI (100 μg mL^{-1}) for 10 min at 37 °C. The cells were then washed thrice and observed by using a confocal laser scanning microscope (CLSM, Zeiss 710 META, Germany).

For the quantitative analysis of cellular uptake, the cells were seeded into a 6-well plate at a density of 1×10^5 cells per well, followed by incubation overnight. The cells were treated by using similar methods as above described (except at a DOX concentration of 10 μg mL^{-1}), then digested with trypsin, harvested, re-suspended in PBS and determined using a flow cytometer (BD FACSCalibur, USA). The DOX content in the cells was also determined by HPLC assay and calculated according to the following formula: DOX content (μg mg^{-1}) = $Q_{DOX}/Q_{cell\ protein}$, where Q_{DOX} and $Q_{cell\ protein}$ are the content of DOX and the total cell protein, respectively. At the end of the experiment, the cells were washed three times with cold PBS and then lysed with 200 μL of cell lysis buffer containing PMSF. The cell lysate was centrifuged at 12 000 rpm for 10 min. 100 μL of the supernatant was extracted with chloroform, evaporated and re-dissolved in methanol for HPLC analysis. 20 μL of the supernatant was used for BCA assay.

2.9. Bio-TEM of cells

When incubated with pretreated RGD-sNPs (MMP9 for 12 h) for 2 h or 4 h, the cells were fixed with 2.5% glutaraldehyde at 4 °C for 15 min, and then separated with a cell scraper, followed by centrifugation for 5 min at 3000 rpm and storage at 4 °C with a fixative for at least 4 h. The cell pellet was then washed thrice with 0.1 M PBS (pH 7.4), each time for 15 min. Next, the cell pellet was incubated with 0.1 M PBS containing 1% osmium tetroxide for 2 h at room temperature, and subsequently washed with 0.1 M PBS (pH 7.4) three times as mentioned above and dehydrated with a serial gradient of 30%, 50%, 70%, 80%, 85%, 90%, 95% and 100% ethanol (10–15 min per time). Thereafter, it was successively infiltrated with a mixture of ethanol and EPON 812 resin three times at different ratios of 2 : 1 and 1 : 1, and pure EPON 812 resin. The experimental temperature was set at 37 °C and each time for 8–12 h. The sample was polymerized for 48 h at 60 °C and then cut into ultrathin sections with a thickness of 80–100 nm by using a microtome (Leica, EM UC7, Germany). The section was stained with a U-Pb double staining method (1% osmic acid for 1 h and 4% uranyl acetate for 15 min, respectively). After drying overnight, the sample was observed by using a TEM (Tecnai G2 F20 TWIN, FEI, USA) at an acceleration voltage of 200 kV.

2.10. *In vitro* cytotoxicity assay

The *in vitro* cytotoxicity was evaluated in HepG2, MCF-7, 4T1, MCF-7/ADR and H22 cell lines. In brief, the cells were seeded at a density of 5.0×10^3 cells per well in 96-well plates. After 24 h of incubation, the cells were treated with free DOX, RGD-nNPs, RGD-sNPs, pretreated RGD-sNPs (RGD-sNPs pretreated with MMP9 for 12 h) and pretreated 2-(Nap)-FFKAGLDD-RGD (peptide 1, NapFFK-RGD, in a similar molar ratio of DOX, pretreated with MMP9 for 12 h) at an equivalent concentration of DOX ranging from 0.1 to 10 μg mL^{-1} for another 24 h or 48 h, followed by the addition of 20 μL of the MTT solution (5 mg mL^{-1}). Four hours later, the medium was removed and 150 μL of DMSO was then added. The absorbance values were determined at 570 nm by using a microplate reader (Thermo Scientific, USA), and the half maximal inhibitory concentration (IC_{50}) was also calculated using SPSS15 software.

2.11. *In vitro* tumor penetration in multicellular tumor spheroids (MCTs)

The MCTs of both HepG2 and 4T1 cells were developed by a liquid overlay method.[40] In brief, each well of a 96-well plate was previously coated with 80 μL of sterile 1% (w/v) agarose in 1 M PBS to generate a non-adherent surface. 200 μL of HepG2 cell (2×10^3 cells per well) or 4T1 cell (5×10^3 cells per well) suspensions were seeded into each well, and then maintained in a 37 °C humidified incubator with 5% CO_2 for 6–8 days until the diameter of the MCTs reached 400–500 μm. The uniform and compact MCTs were selected and carefully transferred to a confocal disk for further study.

The selected MCTs were incubated with free DOX, RGD-nNPs, pretreated RGD-sNPs (RGD-sNPs pretreated with MMP9 for 12 h) and untreated RGD-sNPs at an equal DOX concentration of 20 μg mL^{-1}, respectively. After incubation, the MCTs were washed thrice and fixed with 4% PFA for 30 min, and subsequently washed and observed by CLSM using *Z*-stack imaging from the top to the equatorial plane of the MCTs at intervals of 20 μm.

2.12. The establishment of tumor models and the expression levels of MMP9 in different tumors

The MMP9 levels in different tumors were first determined. To establish the S180 and H22 sarcoma models, 200 μL of cell suspension in 0.9% NaCl (5×10^6 cells) was inoculated in the right flank of female Kunming mice. The MCF-7/ADR tumor model was constructed by subcutaneously inoculating the flank region of female BALB/c nude mice with 5×10^6 cells in a serum-free medium. In the LLC and B16F10 tumor models, 5×10^6 and 1×10^4 cells were subcutaneously injected in the back of C57BL/6 mice, respectively. To set up the 4T1 *in situ* tumor model, 100 μL of cell suspension in PBS was subcutaneously inoculated in the right mammary gland of BALB/c mice. The tumor length (L) and width (W) were measured and the tumor volume (V) was calculated with the following formula: $V = L \times W^2/2$. When the tumor volume reached 200–300 mm^3, the tumor was resected, rinsed with PBS and fixed in 4% PFA for immunohistochemical (IHC) analysis.

2.13. *In vivo* imaging and drug retention

When the tumors reached 200–300 mm^3, Cy7.5-RGD-nNPs or Cy7.5-RGD-sNPs were administered *via* the tail vein at an equal

Cy7.5 dose of 100 μg per mice, respectively. At pre-determined time intervals, the mice were imaged by using an IVIS Lumina imaging system (Caliper, USA). At 96 h post injection, the tumors and main organs were collected, rinsed with PBS, weighed and imaged. The *in vivo* and *ex vivo* fluorescence intensities in the tumors and main organs were both analyzed by a region-of-interest method using Living Image Software.

To directly monitor the DOX retention in the tumor site, H22 tumor-bearing mice with a tumor volume of 200–300 mm^3 were intravenously injected with free DOX, RGD-nNPs and RGD-sNPs at a DOX dose of 5 mg kg^{-1}, respectively. At designed time points, mice were sacrificed and the tumors were resected, washed and weighed. The tumors were cut into pieces and then homogenized in PBS in an ice bath. DOX was extracted with a triple volume of chloroform/isopropylalcohol (1 : 1, v : v), and the organic phase was collected by centrifugation at 12 000 rpm for 15 min and evaporation. The DOX concentration was measured by HPLC as described above. % ID g^{-1} was calculated with the following equation: % ID g^{-1} = $Q_c/(Q_i \times Q_t) \times 100\%$, where Q_c, Q_i, and Q_t are the DOX content in the tumor site, the injected dose of DOX and the weight of the tumor, respectively. The retention of RGD-sNPs in the 4T1 tumor site was also evaluated. In addition, frozen section analysis was also performed to observe the DOX retention in the tumors at the end of the experiment.

The Bio-TEM of tumor tissues was performed according to a similar method as described above to evaluate the *in situ* formation of nanofibers mediated by MMP9.

2.14. *In vivo* tumor penetration

The *in vivo* tumor penetration of RGD-nNPs and RGD-sNPs was evaluated in both H22 and 4T1 tumor models relying on previously described methods.[40] When the tumor reached 200–300 mm^3, RGD-nNPs or RGD-sNPs were intravenously administered at an equal DOX dose of 2.5 mg kg^{-1}. At 48 h post administration, the tumors were excised and rinsed with ice-cold PBS, followed by cryotomy. The frozen tumor sections were stained with the FITC-CD31 antibody, and subsequently observed and photographed under a fluorescence microscope. To further estimate the *in vivo* tumor penetration, RGD-nNPs or RGD-sNPs were intratumorally injected at an equally fixed depth of 3 mm under the surface of the tumors. At 48 h post-injection, the tumors were excised, washed and stored at −80 °C for further analysis. The frozen sections were performed at different layers from the top of the tumor to the middle by cryotomy, followed by DAPI staining for cell nuclei and observation by fluorescence microscopy.

2.15. *In vivo* antitumor efficacy

When the volume of the H22 tumor was around 50–70 mm^3, the tumor-bearing mice were randomly divided into five groups (n = 8) and treated with saline, free DOX (i.v., 2.5 mg kg^{-1}), RGD-nNPs (i.v., 2.5 mg kg^{-1} for DOX), RGD-sNPs (i.v., 2.5 mg kg^{-1} for DOX) and NapFFK-RGD (i.v., at an equal molar amount of DOX, 6 mg kg^{-1}) 4 times at 3-day intervals. The tumor volumes, the general state of experimental mice and the body weight were monitored every other day. At the end of the experiment, the mice were sacrificed. The blood samples, tumors and main organs were collected. Three of the tumors were collected and stored at −80 °C, and the others were fixed in 4% PFA. The tumor inhibition ratio (TIR) was calculated with the following formula: TIR (%) = $(W_s - W_e)/W_s \times 100\%$, where W_e is the mean tumor weight of the experimental groups and W_s is that of the saline group. The blood samples were centrifuged at 3000 rpm for 10 min and the plasma was then obtained and stored at −20 °C for safety evaluation. The hematological and biochemical parameters were determined by using the corresponding assay kits. The tumors and main organs were subjected to hematoxylin–eosin (H&E) staining, IHC analysis including terminal deoxynucleotidyl transferase mediated UTP end labeling (TUENL) and caspase-3 staining. The survival rate of H22 tumor-bearing mice was investigated in an independent study and the mice were divided into three groups (n = 10, free DOX, RGD-sNPs and RGD-nNPs). After treatment four times, the number of survived mice was counted. The *in vivo* antitumor efficacy was also determined in the 4T1 *in situ* tumor model by using similar methods (n = 8). The mice were divided into four groups (n = 8) and treated with saline, free DOX (i.v., 2.5 mg kg^{-1}), RGD-nNPs (i.v., 2.5 mg kg^{-1} for DOX) and RGD-sNPs (i.v., 2.5 mg kg^{-1} for DOX) 4 times at 3-day intervals.

2.16. Statistical analysis

The data were all shown as mean ± SD. Statistical analysis was conducted through two-tailed Student's t-test or one-way ANOVA using SAS9.1 statistical software, with $^*p < 0.05$ as statistically significant difference and with $^{**}p < 0.01$ as extreme significance.

3. Results and discussion

3.1. Preparation and characterization of RGD-sNPs and RGD-nNPs

Compounds **1** and **2** were synthesized by firstly modifying the peptide (MMP9-sensitive peptide 1: 2-(Nap)-FFKAGLDDRGD and MMP9 non-sensitive peptide 2: 2-(Nap)-FFKWGLWGRGD) with TPA-NHS, which preferentially reacted with $-NH_2$ of lysine (Lys, K) in the peptide skeleton, and then reacting with DOX through the formation of a pH-sensitive hydrazine bond. The facile synthetic route is shown in Fig. S5 and S6.† The target products were purified by semi-preparative high pressure liquid chromatography and characterized by HPLC (Fig. S7†), and were determined to be more than 96%. HRMS of compound **1** (Fig. S8, ESI†) m/z: ($[M + H]^+$) calcd for $C_{102}H_{120}N_{16}O_{31}$, 2067.1382; found 2067.3329. HRMS of compound **2** (Fig. S10, ESI†) m/z: ($[M + H]^+$) calcd for $C_{117}H_{130}N_{18}O_{29}$, 2253.3873; found 2253.6764. The ^{1}H-NMR spectra of compounds **1** and **2** both showed characteristic peaks of DOX and peptide skeletons, as labelled in Fig. S9 and S11.† The above results indicated that compounds **1** and **2** were both successfully synthesized with high purity.

The CAC values of compounds **1** and **2** were further determined to estimate their self-assembly ability. The CAC values were 60.3 μg mL^{-1} and 51.4 μg mL^{-1}, respectively, which would ensure the formation of stable nanoparticles.[41] They can self-assemble into nanoparticles (RGD-sNPs and RGD-nNPs, respectively) in a neutral environment (pH 7.4, 1 M PBS) by a modified rapid precipitation method.[30] 20 μL of the conjugate solution (DMSO, 50 mg mL^{-1}) was rapidly injected into 980 μL PBS under stirring, and the assembly occurred automatically. This was mainly attributed to the intermolecular π–π stacking, strong hydrophobic interaction and *J*-type aggregation, which would facilitate a thermodynamically stable state with the lowest energy in the process of the self-assembly.[41–43] To further validate the formation of nanoparticles, the DLS and TEM measurements were performed (Fig. 1a and b). RGD-sNPs and RGD-nNPs both displayed a spherical shape with hydrodynamic diameters of 45.7 ± 5.4 nm and 41.2 ± 9.8 nm, and with slightly negative charges of −8.44 ± 1.4 mV and −7.12 ± 1.1 mV, respectively. The suitable size and surface charge can contribute to the passive targeting and long circulation of nanoparticles. It has been reported that nanoparticles with a size >5 nm and <100 nm can achieve considerable accumulation *via* an EPR effect, and simultaneously avoid renal clearance and RES capture.[36,41] In addition, RGD-sNPs and RGD-nNPs both showed good physiological stability in PBS (pH 7.4) containing 10% FBS at 37 °C for 48 h (Fig. S12†).

3.2. Structural transformation of RGD-sNPs

To verify the structural transformation of RGD-sNPs, the freshly prepared nanoparticles were dispersed and incubated with pH 6.8 PBS containing 50 ng mL^{-1} MMP9 at 37 °C for different times. The enzymatic cleavage behavior and selective cutting site was firstly evaluated by HPLC and HRMS. As shown in Fig. 1d and Fig. S13,† the enzymatic responsive linker can be effectively broken by MMP9 and be completely digested within 12 h, generating the 2-(Nap)-$FFK_{TPA\text{-}DOX}AG$ residue as evidenced by HRMS (ESI): *m*/*z* ($[M + H]^+$) calcd for $C_{76}H_{79}N_7O_{19}$, 1394.4760; found 1394.5464. Its chemical structure is displayed in Fig. S14.† DOX was also detected, but in lower quantities (<10%), indicating that the formed hydrazone bond was relatively stable during the process of structural transformation at pH 6.8. The TEM, DLS and circular dichroism (CD) spectroscopy experiments were also carried out to investigate the morphological changes and secondary structure of the aggregates. As shown Fig. 1a, spherical nanoparticles were gradually transformed into rod-like nanoparticles (S-NFs) with an average diameter of 18 ± 1.6 nm and length of 225.7 ± 10.2 nm, during the experimental time of 12 h. They were conducive to deep tissue penetration and accelerated internalization.[24–26] The DLS data also showed that the particle size increased to 318.8 ± 14.3 nm after 12 h of treatment (Fig. 1b). RGD-nNPs had no enzyme responsiveness with any change in particle size and morphology when treated with MMP9 at the same concentration (Fig. 1a). The CD spectra of both RGD-sNPs and RGD-nNPs showed no evidence of a remarkable secondary structure. After 12 h of treatment with MMP9, there was obvious H-bonding β-sheet structure formation regardless of the morphology, as evidenced by a positive peak at 196 nm and a negative one at 216 nm (Fig. 1c, Fig. S15†). Furthermore, RGD-sNPs incubated with MMP9 exhibited a nearly 12-fold stronger negative signal at 216 nm than that of RGD-nNPs, which probably revealed that there was more hydrogen bond formation in the fibrous morphology.[30,44] The weak acid triggered shape transformation process of S-NFs and RGD-nNPs was then monitored. After continuous incubation in a pH 5.5 environment for 24 h, S-NFs were changed into longer fibers with a mean particle size of >5 μm as confirmed by TEM and DLS (Fig. 1a and b). The characteristic signal of ordered β-sheet structure generation was still observed and was much stronger (Fig. 1c). However, the spherical structure of RGD-nNPs almost disappeared when they encountered a pH 5.5 environment within 24 h, and the particle size was undetectable with an extremely low count rate by DLS (Fig. 1a). The results were ascribed to the cleavage of a pH-sensitive hydrazine bond, which simultaneously demonstrated that the physical mixture of DOX and peptide **2** was incapable of assembling into ordered nanostructures, such as nanoparticles or others.

3.3. *In vitro* drug release

We further evaluated the pH-responsive drug release kinetics of RGD-nNPs, RGD-sNPs and S-NFs over time at pH 7.4, 6.8 and 5.5. As shown in Fig. 2a and b, only about 15% of DOX was released from RGD-nNPs and RGD-sNPs within 24 h, and approximately 20% was released within the experimental time of 96 h at pH 7.4. In a pH 6.8 environment, the cumulative DOX release was slightly increased up to 36% within 96 h in both RGD-nNPs and RGD-sNPs, but only around 26% in S-NFs. The results indicated that DOX release was relatively slow in fibrous morphologies, which may contribute to the stability of nanofibers in the tumor microenvironment. In contrast, nearly 40% of DOX was released in the initial 4 h and the cumulative release reached up to more than 80% within 24 h at pH 5.5. DOX was rapidly released from S-NFs at pH 5.5 as well, with around 70% cumulative DOX release within 48 h. The results demonstrated that the nano-preparation assembled by peptide–DOX prodrugs was relatively stable under physiological conditions and could quickly release DOX in a weakly acidic intracellular environment no matter in spherical or rod-like fibrous morphologies.

3.4. *In vitro* cellular uptake and cytotoxicity

The enhanced cellular uptake of nanofibers was then examined in HepG2 and 4T1 cell lines. As shown in Fig. 3a, free DOX could be easily internalized in HepG2 cells and subsequently enter the nucleus as confirmed by a strong red fluorescence signal in the nucleus at 4 h, and the signal became much stronger at 24 h. However, nanoparticles (both RGD-sNPs and RGD-nNPs) were mainly located in the cytoplasm 4 h post incubation, no matter pretreated with MMP9 or not (Fig. 2a, Fig. S16†). It may be attributed to the fact that nanoparticles were internalized by cells through the endocytic

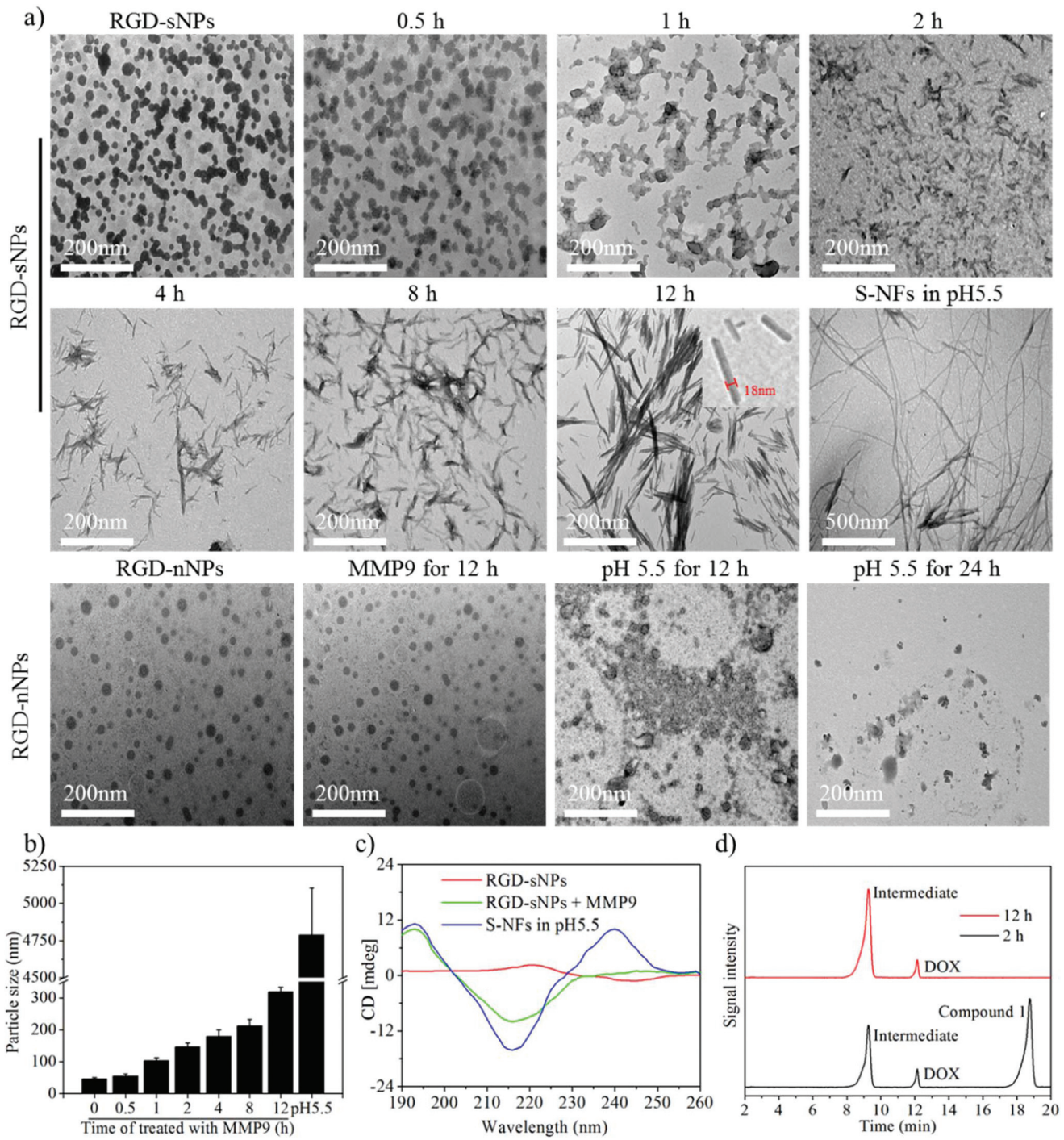

Fig. 1 The characterization of the spherical nanoparticles RGD-sNPs and RGD-nNPs under different conditions. (a) TEM images of RGD-sNPs treated with MMP9 for 0, 0.5, 1, 2, 4, 8, and 12 h, and of S-NFs in pH 5.5 PBS for 24 h. TEM images of RGD-nNPs under different conditions. (b) Particle size change of RGD-sNPs under different conditions. (c) CD spectra of RGD-sNPs, pretreated RGD-sNPs (pretreated MMP9 for 12 h) and S-NFs (incubated in pH 5.5 PBS for 24 h). (d) The HPLC spectra of RGD-sNPs treated with MMP9 for 2 h and 12 h, respectively.

pathway, and thus they must initially escape from the lysosome and then distribute in the whole cells. As displayed in Fig. 3b and Fig. S17,† rod-like nanoparticles with a length of about 300 nm were clearly observed in the intracellular vesicles or endosomes after 2 h or 4 h of incubation with pretreated RGD-sNPs, suggesting that they were probably internalized by cells *via* endocytosis.[17] At 24 h post co-incubation, a DOX fluorescence signal was widely observed in the cells, especially in the blue fluorescent nuclei, indicating that the nanoparticles had effectively escaped from the *endo*-lysosomes. Importantly,

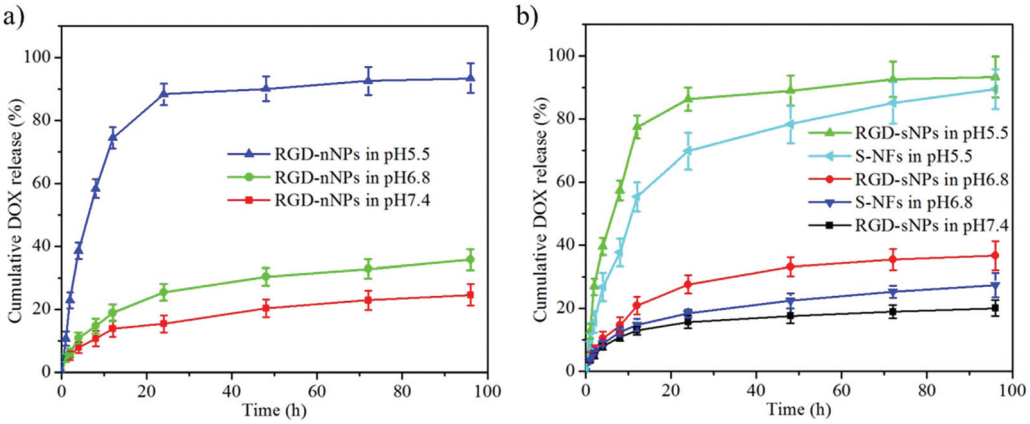

Fig. 2 Cumulative drug release of RGD-nNPs, RGD-sNPs and S-NFs. (a) Cumulative drug release of RGD-nNPs at pH 7.4, 6.8 and 5.5 (n = 3). (b) Cumulative drug release of RGD-sNPs at pH 7.4, 6.8 and 5.5, and of S-NFs at pH 6.8 and 5.5 (n = 3).

RGD-sNPs that were pretreated with MMP9 for 12 h (RGD-sNPs + MMP9 group) exhibited much higher intracellular fluorescence intensity in both the cytoplasm and nuclei, compared with that of unpretreated RGD-sNPs. Quantitative analysis by flow cytometry and HPLC substantiated that the RGD-sNPs + MMP9 group provided around 2-fold higher DOX accumulation in HepG2 cells compared to the unpretreated RGD-sNPs group (Fig. 3c). The increased intracellular accumulation suggested that rod-like nanoparticles (S-NFs) with a suitable size can indeed facilitate cellular uptake. In addition, the average diameter of the nucleopores was reported as ~39 nm, and thus the formed S-NFs can freely access the nuclear compartment by the way of passive diffusion, resulting in increased accumulation in the nucleus.[45,46] A similar phenomenon was also observed in 4T1 cells (Fig. S18†). It is noteworthy that the relative DOX intensity calculated by flow cytometry was significantly higher than the relative DOX amount determined by HPLC at 4 h, but they were approximately equal at 24 h (Table 1). It was probably due to the delayed release of DOX. The experiment of Bio-TEM was performed to further validate the cellular uptake of nanofibers.

In parallel, the cytotoxicity of nanoparticles and nanofibers Q11 were evaluated in four cell lines including HepG2, 4T1, MCF-7, MCF-7/ADR and H22 cells. Free DOX showed the highest cytotoxicity against HepG2 cells after 48 h of treatment, with an IC_{50} value of 0.24 μg mL^{-1} (Fig. 3d and Table 2). Pretreated 2-(Nap)-FFKAGLDDRGD (NapFFK-RGD, pretreated with MMP9 for 12 h) showed modest cell killing ability on HepG2, 4T1, MCF-7 and H22 cells, and significantly higher cytotoxicity against drug-resistant MCF-7/ADR cells than that of free DOX. It has been reported that NapFFKAG (the residue cleaved from NapFFK-RGD treated with MMP9) can self-assemble into long nanofibers or nanogels (NapFFK-NFs, length >5 μm).[35,47,48] More importantly, the formed NapFFK-NFs have an effect on the inhibition of tumor cell growth, migration and invasion.[30,47,48] They can form a network like artificial extracellular matrix (AECM) on the surface of cells, resulting in the inhibition of cellular physiological activity.[30] In addition, they can also induce cell apoptosis through the caspase-3 apoptotic pathway and promiscuous interaction with microtubules in cells.[18,33,47] Compared to RGD-nNPs and untreated RGD-sNPs, pretreated RGD-sNPs (RGD-sNPs + MMP9 group) remarkably reduced the cell viability of experimental cell lines, even in drug-resistant MCF-7/ADR cells. The superior cytotoxicity can be explained by the enhanced cellular uptake and synergistic effect of NapFFK-NFs. Moreover, the transformed rod-like nanoparticles that have the ability to freely access the nucleus can be directly delivered into the nucleus and thus inhibit drug efflux, which may play a significant role in the decreased cell viability of drug-resistant MCF-7/ADR.[46]

Finally, the cell viability of RGD-sNPs and RGD-nNPs against the normal cell line L929 was evaluated, and the IC_{50} values are shown in Table S1.† The results indicated that the nanoparticles assembled from both compounds **1** and **2** were non-sensitive to the normal cell line L929, and the IC_{50} values were extremely higher than that of cancer cells, revealing their safety to healthy cell lines and specific tumor cell killing Q12 ability.

3.5. *In vivo* imaging and drug retention

Rod-like nanoparticles have been reported to notably prolong the drug retention time in the tumor site.[12,49] To investigate the prolonged drug retention and *in situ* structural reconstruction induced by MMP9, the expression level of MMP9 in various tumor types was firstly detected by the IHC analysis method. As depicted in Fig. S19,† MMP9 was overexpressed in B16F10 melanoma, H22 hepatoma and S180 sarcoma, but rarely expressed in the triple negative breast cancer (4T1), drug-resistant human breast cancer (MCF-7/ADR) and Lewis lung carcinoma (LLC) tumor models. Accordingly, H22 hepatoma was constructed to evaluate the targeting ability, retention and structure transformability of RGD-sNPs, with the 4T1 orthotopic tumor model as a control. Besides, Cy7.5-labeled RGD-sNPs (Cy7.5-RGD-sNPs) and RGD-nNPs (Cy7.5-RGD-nNPs) were prepared by a similar method and their *in vitro* morphological changes triggered by MMP9 were

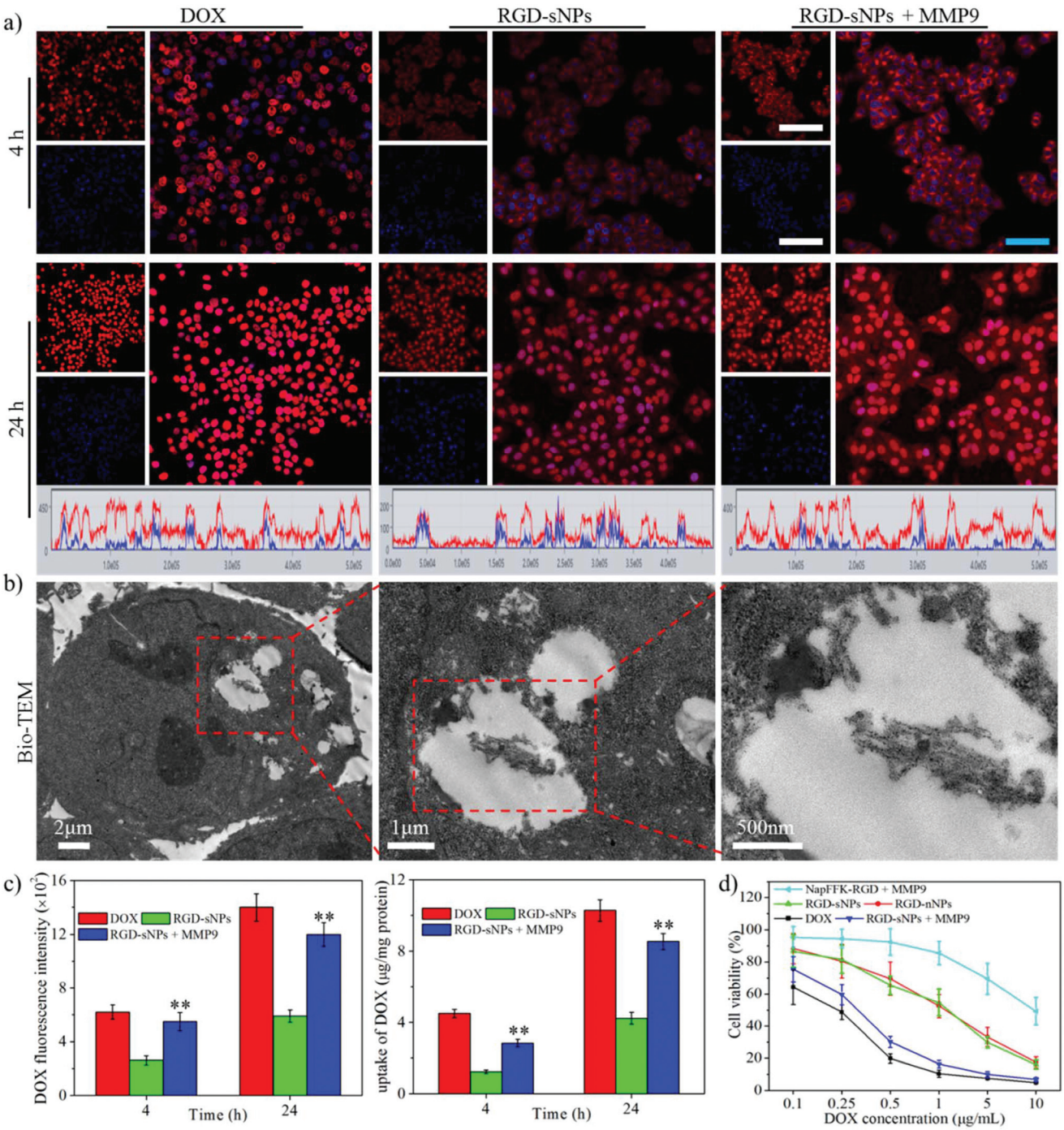

Fig. 3 The enhanced cellular uptake and cytotoxicity. (a) Confocal laser scanning microscopy (CLSM) images of cellular uptake in HepG2 cells incubated with free DOX, RGD-sNPs and pretreated RGD-sNPs (pretreated MMP9 for 12 h) for 4 h or 24 h (white scale bar for 100 μm and blue scale bar for 50 μm). The blue nuclei were stained with DAPI. (b) Bio-TEM images of HepG2 cells. Cells were incubated with pretreated RGD-sNPs (pretreated MMP9 for 12 h) for 4 h. (c) Quantitative analysis of DOX fluorescence intensity by flow cytometry and the amount of DOX internalized by HepG2 cells determined by HPLC (n = 3), $^{**}p < 0.01$ *vs.* the RGD-sNPs group. (d) Cell viability of HepG2 cells after 48 h of incubation with free DOX, RGD-nNPs, RGD-sNPs, pretreated RGD-sNPs (pretreated MMP9 for 12 h), and pretreated NapFFK-RGD (MMP9 for 12 h).

also confirmed by TEM (Fig. S20†). The biodistribution of Cy7.5-RGD-sNPs and Cy7.5-RGD-nNPs injected intravenously into tumor-bearing mice was monitored by using an *in vivo* imaging system. The *in vivo* imaging results demonstrated that both can be efficiently accumulated in the tumor region as a result of the combination of passive and active targeting mechanisms (Fig. 4a). Cy7.5-RGD-sNPs showed a relatively considerable accumulation at the H22 tumor site over 96 h

Table 1 The DOX intensity and DOX amount internalized in HepG2 cells (n = 3)

Groups	4 h		24 h	
	DOX intensity[a]	DOX amount[b]	DOX intensity	DOX amount
DOX	—	—	—	—
RGD-sNPs	0.42	0.27	0.43	0.41
RGD-sNPs + MMP9	0.89	0.63	0.86	0.83

[a] The DOX fluorescence intensity ratio of nanoparticles to free DOX. [b] The uptake DOX amount ratio of nanoparticles to free DOX.

Table 2 The IC_{50} values of DOX and nanoparticles against cancer cells after 48 h of treatment (n = 6)

Groups	IC_{50} values[b] ($\mu g\ mL^{-1}$)				
	HepG2	4T1	MCF-7	MCF-7/ADR	H22
DOX	0.24	0.56	0.34	41.45	0.38
RGD-nNPs	1.37	2.04	1.78	68.45	2.14
RGD-sNPs	1.32	1.75	1.41	59.99	2.23
RGD-sNPs + MMP9[a]	0.31**	0.78**	0.45**	2.74**	0.42**
NapFFK-RGD[a]	10.07	24.56	11.08	15.27	19.87

[a] Treated with MMP9 for 12 h. [b] The half maximal inhibitory concentration. **$p < 0.01$ *vs.* the RGD-sNPs and RGD-nNPs groups.

with the maximum fluorescence intensity at 24 h post-injection (Fig. 4a). The long-term retention of Cy7.5-RGD-sNPs was probably ascribed to the structural transformation of nanoparticles into nanofibers triggered by high-level MMP9. As can be seen in Fig. 4b and Fig. S21,† *in situ* formed rod-like nanoparticles were clearly found in the H22 tumor tissue section after 24 h of administration of Cy7.5-RGD-sNPs. By contrast, the non-transformable Cy7.5-RGD-nNPs were almost entirely cleared from the tumors after 48 h, which was frequently observed for targeted polymeric nanoparticle accumulation and elimination in tumor-bearing mice.[30,50] Similarly, a very weak fluorescence signal was observed at the tumor site in 4T1 tumor-bearing mice treated with Cy7.5-RGD-sNPs for 48 h (Fig. 4a). It was because of the low expression level of MMP9 leading to no or fewer rod-like nanoparticles formed in the tumors. Quantitative analysis of the fluorescence intensity at the tumor site showed a similar tendency and further provided evidence of the markedly extended retention time of *in situ* converted nanofibers (Fig. S22†). At 96 h post-administration, the tumors and main organs were harvested, rinsed and imaged. As shown in Fig. 4a, the strongest fluorescence signal was observed in the tumors resected from H22 tumor-bearing mice treated with Cy7.5-RGD-sNPs, and was significantly higher than that in normal tissues. Quantitative assessment indicated that Cy7.5-RGD-sNPs showed around 29-fold higher fluorescence in H22 tumors compared to that of Cy7.5-RGD-nNPs (Fig. 4c). Additionally, the intratumoral pharmacokinetics study of DOX was performed to continue exploring the targeted accumulation and extended retention of transformable RGD-sNPs in the tumors. As shown in Fig. 5, free DOX achieved the highest drug concentration in the tumors at 4 h post-administration, and was rapidly eliminated due to its poor pharmacokinetic characteristics. The DOX amount in the tumor tissues of the nanoparticle groups was notably higher compared to free DOX during the experimental period, indicating that the biodistribution and retention of free DOX can be indeed optimized through a nano-enabled drug design method. Importantly, transformable RGD-sNPs were able to obtain the most drug accumulation and the longest retention time, with ~15.1% ID g^{-1} at 24 h and even ~3.7% ID g^{-1} at 96 h, respectively. The frozen section results showed that a strong red fluorescence signal was clearly seen and extensively distributed in the tumor tissue (Fig. 4d). These results were highly in line with those acquired by *in vivo* fluorescence imaging. Taken together, the above results revealed that the strategy of combining targeted nanoparticles and *in situ* transformed nanofibers can really achieve the preferred drug accumulation and prolonged retention time in the tumor than in normal organs.

3.6. *In vitro* and *in vivo* penetration of RGD-sNPs

To estimate the deep tissue penetration of *in situ* constructed nanofibers, the multicellular tumor spheroids (MCTs) were first established based on HepG2 and 4T1 cells to simulate solid tumors and monitor the penetration of transformed nanofibers. As shown in Fig. 6, at 8 h post incubation with pretreated RGD-sNPs (pretreated with MMP9 for 12 h), bright DOX fluorescence spread throughout the great portion of HepG2 MCTs, and even at 140 μm from the surface to the central region of MCTs. It was confirmed to penetrate nearly 56% of MCTs that had a diameter of about 500 μm. However, the control groups (RGD-nNPs, untreated RGD-sNPs and free DOX) exhibited red fluorescence of DOX distribution surrounding the HepG2 MCTs, which became negligible at 80 μm depth. Such elevated tumor penetration of transformed nanofibers was also verified in 4T1 MCTs.

Afterwards, the *in vivo* tumor tissue penetration of RGD-sNPs was evaluated in H22 sarcoma and *in situ* 4T1 tumor-bearing mice. After 48 h post-i.v. administration, DOX delivered by RGD-nNPs was distributed around the periphery of blood vessels, as evidenced by the overlaid yellow fluorescence merged by FITC-CD31 and red DOX (Fig. 7a). By comparison, free DOX can be extravasated from the blood vessels and can diffuse to a certain distance (Fig. S23†). It has been proved that small molecule drugs were provided with moderate tumor penetration ability.[30,52,53] Unfortunately, DOX with weak red fluorescence spots scattered in the tumor region, probably due to the nonspecific accumulation and rapid elimination of free DOX as previously confirmed.[53,54] Importantly, transformable RGD-sNPs displayed bright and abundant DOX fluorescence in the H22 tumor tissue section, while faint fluorescence spots remained around the blood vessels in the 4T1 tumor site (Fig. 7a). In order to further verify the enhanced tumor penetration of nanofibers, free DOX and nanoparticles were intratumorally injected into tumor-bearing mice at a fixed depth. As

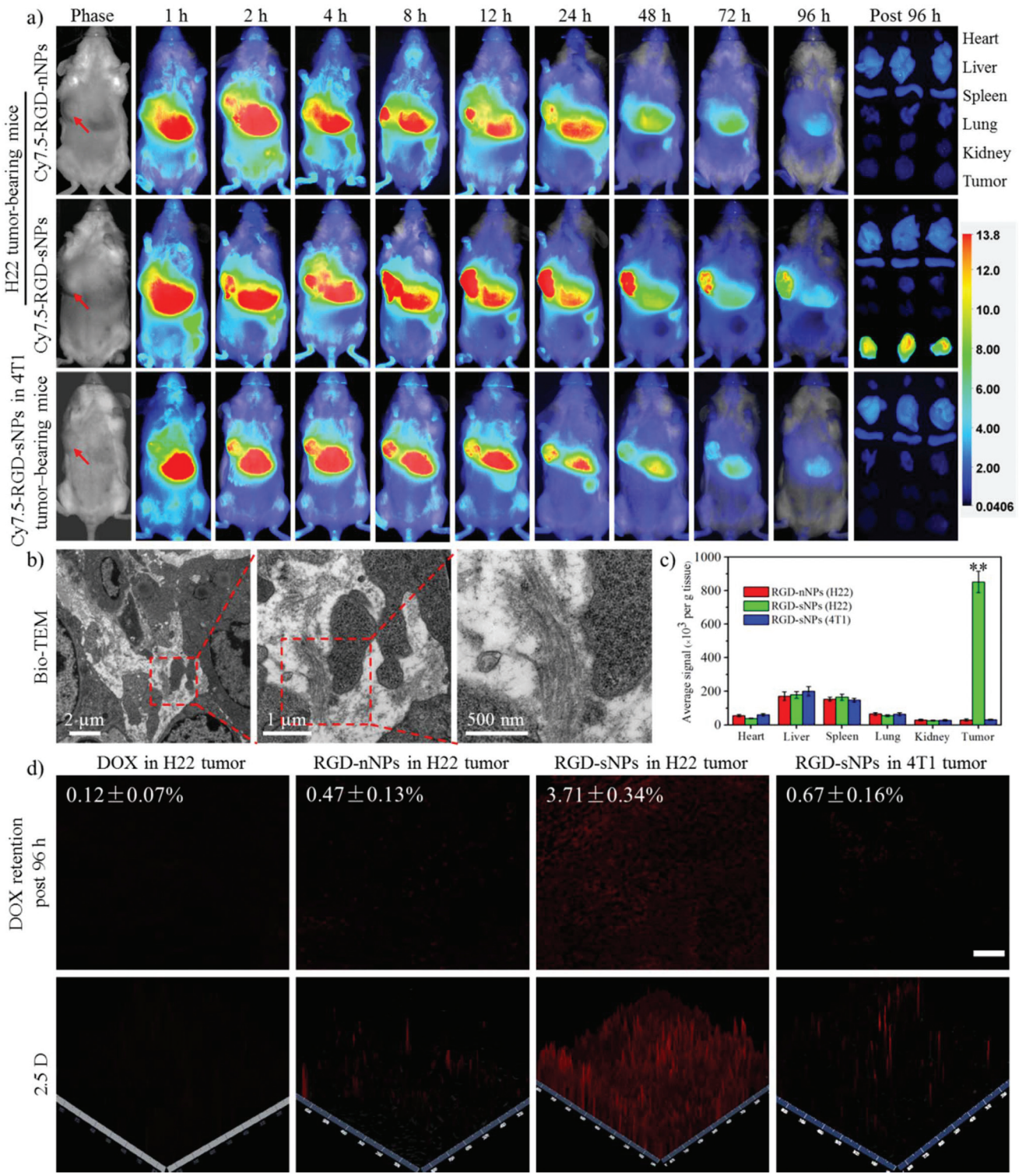

Fig. 4 The improved accumulation and long-term retention of transformable RGD-sNPs. (a) *In vivo* fluorescence imaging of H22 sarcoma and *in situ* 4T1 tumor-bearing mice, and *ex vivo* fluorescence imaging of tumors and normal tissues. The red arrows indicate the tumor regions. (b) Bio-TEM of the tumor tissue section. The tumor was resected from H22 tumor-bearing mice treated with RGD-sNPs for 24 h. (c) The average fluorescence intensity of the tumors and main organs (n = 3), $^{**}p < 0.01$. Average signal (per g tissue) was calculated as the ratio of the total fluorescence intensity to the tissue weight. (d) CLSM examination of DOX retention at the tumor site (scale bar for 100 μm). The frozen sections were prepared using tumors collected from tumor-bearing mice after 96 h of intravenous injection. Mice were intravenously injected with free DOX, RGD-nNPs or RGD-sNPs at a DOX concentration of 5 mg kg^{-1}. The white numbers indicate the DOX amount (DOX/tumor (%ID g^{-1})) in tumors 96 h post i.v. injection, as calculated by HPLC (n = 3). DOX/tumor (% ID g^{-1}) is the ratio of the DOX amount per gram tumor to the total injected dose.

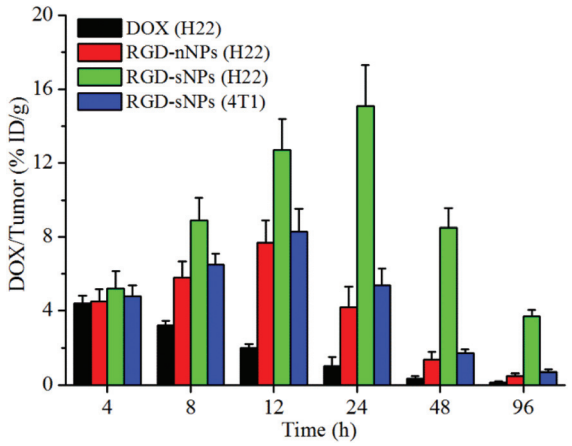

Fig. 5 The DOX concentration in tumors collected from tumor-bearing mice treated with free DOX, RGD-nNPs or RGD-sNPs at a DOX dose of 5 mg kg^{-1}. DOX/tumor (% ID g^{-1}) is the ratio of the DOX amount per gram tumor to the total injected dose (n = 3).

shown in Fig. 7b, transformable RGD-sNPs achieved superior tumor penetration ability with widespread distribution of strong red fluorescence in H22 tumors, even at a depth up to 2000 μm below the injection position, whereas obviously weak DOX fluorescence was detected in the control groups with a depth of 250 μm (Fig. 7b, Fig. S24†). These were highly in accordance with the experimental results obtained by *in vitro* MCTs and intravenous administration. Collectively, drug delivery by an approach of *in situ* transformation of nanoparticles into nanofibers actually boosted deep tumor penetration.

3.7. *In vivo* antitumor efficacy

The antitumor efficacy of RGD-sNPs was evaluated in both H22 sarcoma and *in situ* 4T1 cancer models. Following a tumor volume of ~50–70 mm^3, saline (200 μL), free DOX (2.5 mg kg^{-1}), RGD-nNPs (2.5 mg kg^{-1} for DOX), RGD-sNPs (2.5 mg kg^{-1} for DOX) and NapFFK-RGD (6 mg kg^{-1}, equimolar amount with DOX) were administered intravenously four times at 3-day intervals, respectively. In the H22 sarcoma model, the saline

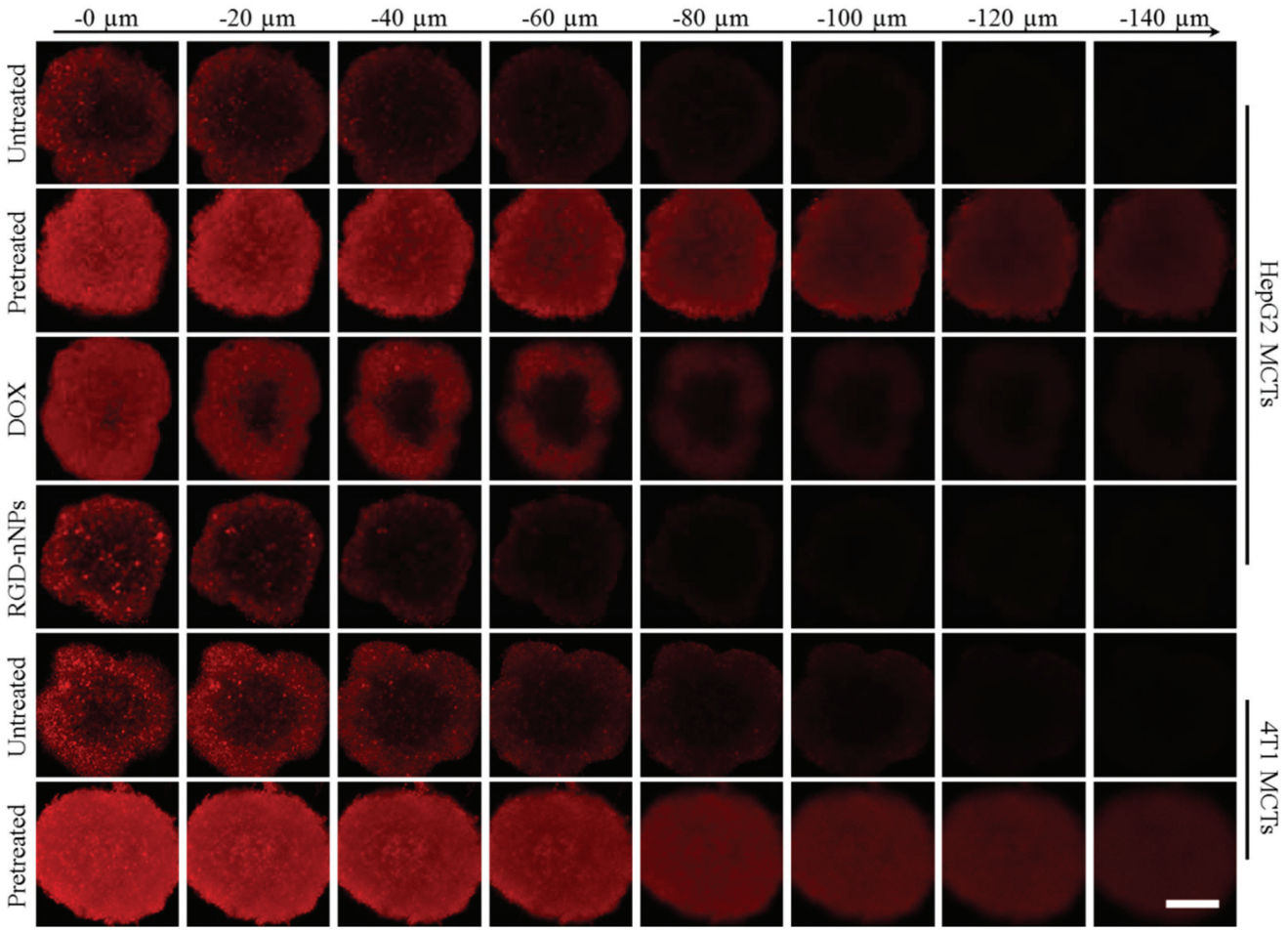

Fig. 6 The *in vitro* penetration of untreated RGD-sNPs, pretreated EGD-sNPs (pretreated with MMP9 for 12 h), free DOX and RGD-nNPs. From the top to the bottom: the *in vitro* penetration of DOX in HepG2 multicellular tumor spheroids (MCTs) after incubation with untreated RGD-sNPs, pretreated RGD-sNPs (pretreated MMP9 for 12 h), free DOX or RGD-nNPs for 8 h at a DOX concentration of 20 μg mL^{-1}, and the *in vitro* penetration of untreated RGD-sNPs and pretreated RGD-sNPs (pretreated with MMP9 for 12 h) in 4T1 MCTs. *Z*-Stack images using CLSM were obtained from the surface to the middle of MCTs at intervals of 20 μm (scale bar for 200 μm).

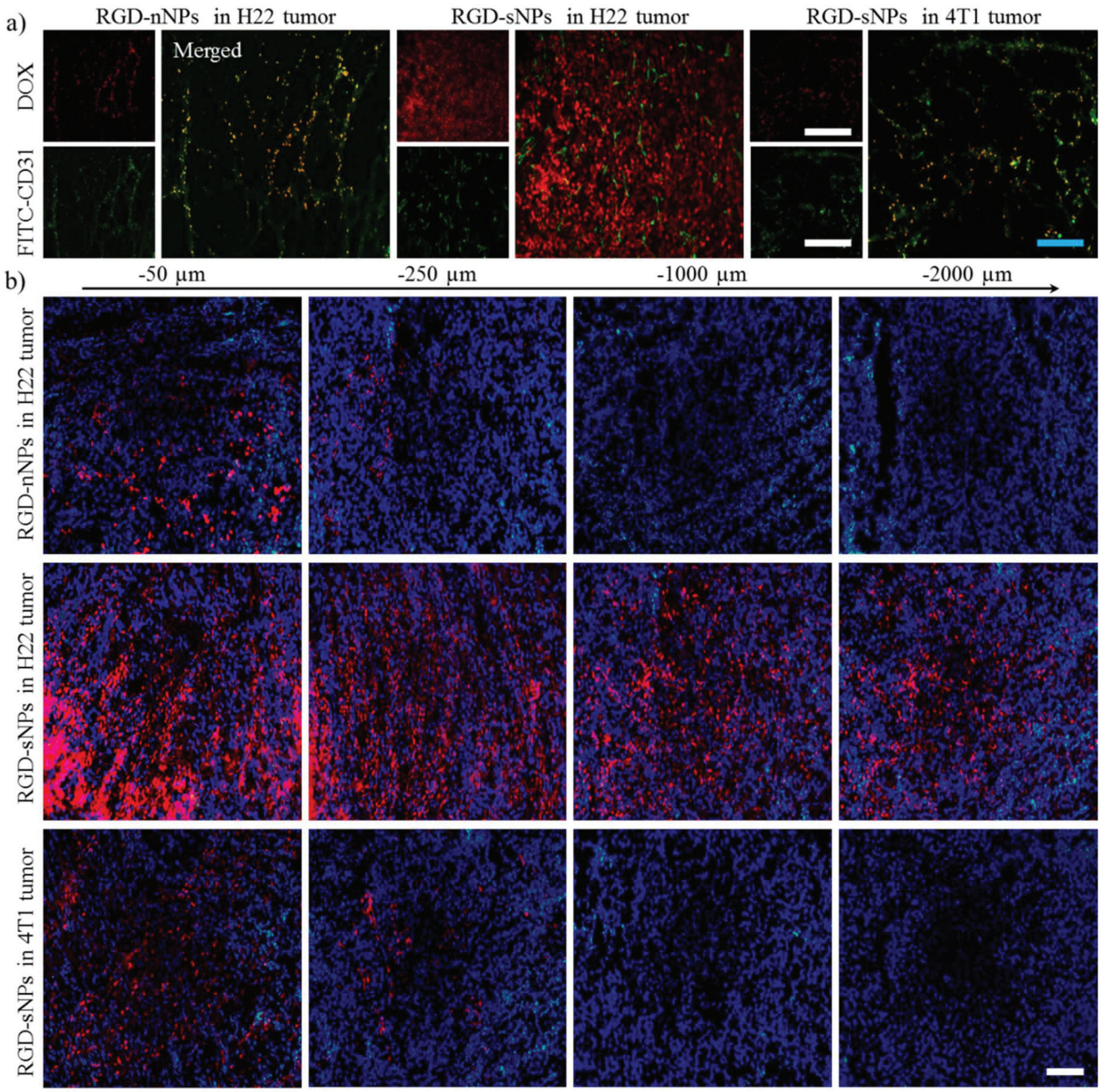

Fig. 7 The *in vivo* penetration of RGD-nNPs and RGD-sNPs. (a) *In vivo* penetration of DOX extravasated from blood vessels after intravenous injection of RGD-nNPs and RGD-sNPs at a DOX dose of 2.5 mg kg^{-1} for 48 h (white scale bar for 200 μm and blue scale bar for 100 μm). (b) *In vivo* penetration of DOX in tumors after intratumoral administration of RGD-nNPs and RGD-sNPs at a DOX dose of 2.5 mg kg^{-1} for 48 h (scale bar for 100 μm). The frozen sections of the tumors were sliced at different depths below the injection position.

group showed an explosive tumor progression with a tumor volume of ~1867 mm^3 and an average tumor weight of 1.72 g at the 18th day post inoculation (Fig. 8a and d). NapFFK-RGD had a modest effect on tumor size reduction with an inhibition rate of 32.6% and a relative apoptotic rate of 15.7% (Fig. 8a and d). The following reasons may be responsible for its tumor inhibitory effect. On the one hand, NapFFK-RGD can form *in situ* self-assembled nanofibers (NapFFK-NFs) like AECM in the tumor microenvironment, which competitively bound to receptors on the surface of cancer cells and subsequently inhibited downstream signal pathways that suppressed tumor growth.[30,52] On the other hand, *in situ* formed NapFFK-NFs can cause apoptosis by the caspase-3 apoptotic pathway and promiscuous interaction with microtubules.[13,47,48] RGD-nNPs and RGD-sNPs both showed significant inhibitory efficacy on H22 tumor growth, compared with free DOX. Importantly, RGD-sNPs possessed the most robust therapeutic effect with the highest tumor inhibition ratio (TIR)

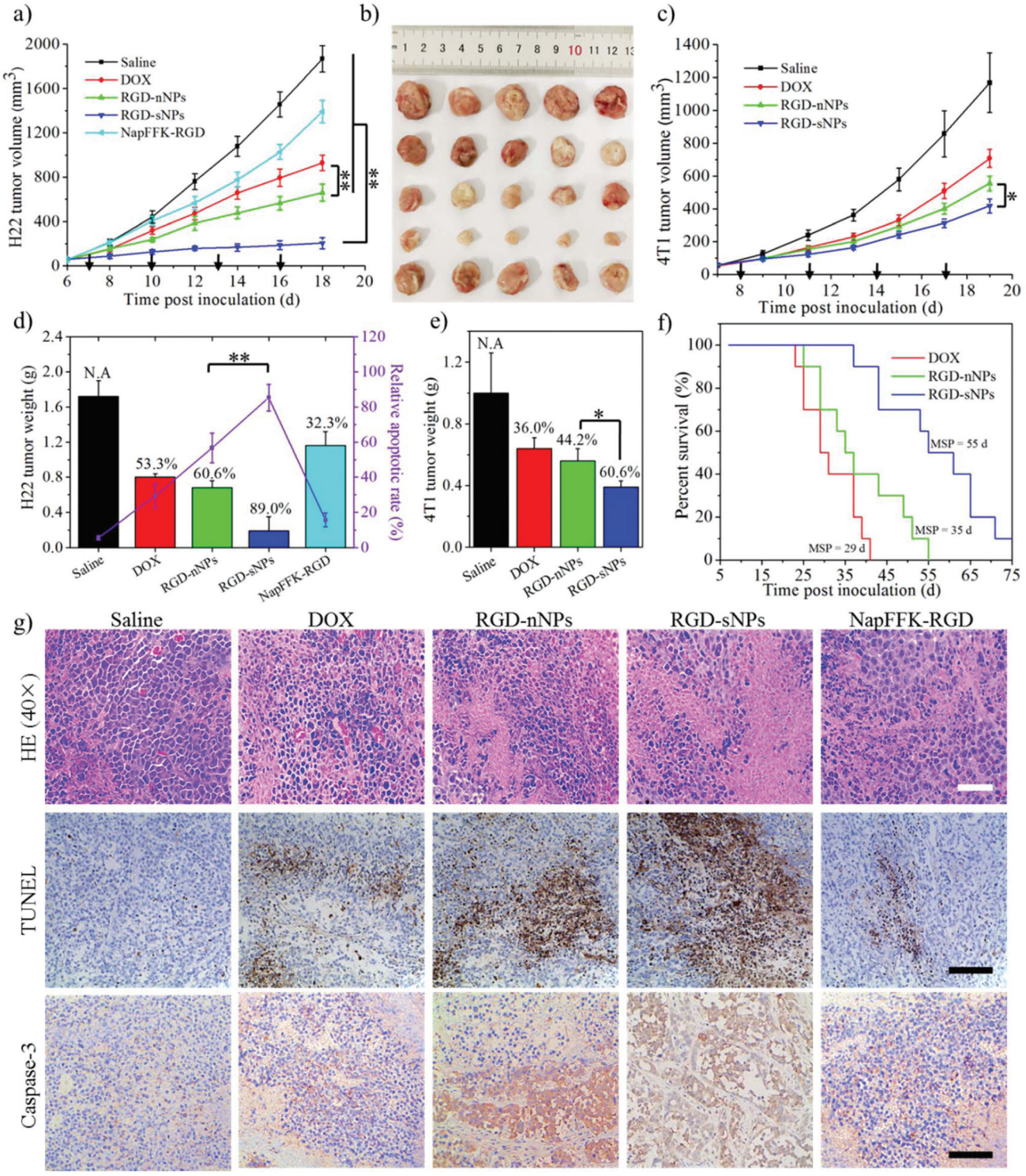

Fig. 8 Antitumor activity in the H22 sarcoma and 4T1 orthotopic tumor-bearing mice. (a) H22 tumor volume curves of mice treated with different formulations as above described (n = 8); the black arrows indicate drug administration, $^{**}p < 0.01$. (b) The image of H22 tumors (5/8) resected after the last treatment; the other three were stored at −80 °C after excision. (c) 4T1 tumor volume curves of mice treated with different formulations as described above (n = 8); the black arrows indicate drug administration, $^{**}p < 0.01$. (d) H22 tumor weight (n = 8) and relative apoptotic rate (n = 3); the numbers on the top of the columns represent the tumor inhibition rate (TIR), $^{**}p < 0.01$. (e) 4T1 tumor weight and relative apoptotic rate; the numbers on the top of the columns represent the TIR, $^{**}p < 0.01$. (f) The percent survival curve of H22 tumor-bearing mice; MSP is the abbreviation of median survival period (n = 10), $^{**}p < 0.01$. (g) Immunohistochemical (IHC) analysis of tumors resected from H22-tumor bearing mice (the white scale bar is 50 μm and the black scale bar is 100 μm).

of 89.0% (Fig. 8b and d). These results were also confirmed by IHC analysis including H&E staining, TUNEL and caspase-3 staining. RGD-sNPs displayed the maximum area necrosis and apoptosis, the largest population of TUNEL-positive cells, and the maximal upregulation of caspase-3 expression (Fig. 8g, Fig. S25†). Meanwhile, the survival rate of H22 tumor-bearing mice was investigated in an independent study. As shown in Fig. 8f, RGD-sNPs notably enhanced the survival time of H22 tumor-bearing mice, approximately doubling the median survival period (MSP) to 55 days, compared with free DOX (with a MSP of 29 days). In comparison with RGD-liposomes and RGD-modified nanogels, the overall survival rate of RGD-sNPs (80 days) was also extended 2- to 3-fold, indicating the superiority of the structure-transformable nanosystems in enhanced cancer therapy.[13,55–57] The best tumor inhibitory effect of RGD-sNPs was largely attributed to their efficient accumulation, extended retention time, deep tissue penetration and enhanced cellular uptake, and the synergistic antitumor effect of NapFFK-NFs as proved above. The superior antitumor effect of RGD-sNPs was also determined in the 4T1 *in situ* cancer model, but the difference was much less marked compared with that of RGD-nNPs (Fig. 8c and e, Fig. S26 and 27†). When mice were treated with RGD-sNPs or RGD-nNPs, they showed a similar trend of tumor growth. This compromised antitumor efficacy of RGD-sNPs in the 4T1 orthotopic tumor model was probably due to the relatively low level of MMP9, so that the nanoparticles cannot be transformed into a fibrous form to comprehensively improve the 'CAPIR cascade'. Thus the results revealed that it is very necessary to confirm the stimuli level in tumors (such as MMP9, MMP2, GSH, pH or ROS) when applying this kind of stimuli-responsive drug release or structure-transformable nanosystem in cancer therapy.

As an indicator of systemic toxicity, the body weight of tumor-bearing mice was monitored during the whole experimental period. As shown in Fig. S28 and 29,† no notable loss of body weight was observed in the saline, RGD-sNPs, RGD-nNPs or NapFFK-RGD group. The body weight of mice treated with free DOX was significantly decreased, almost 20% body weight reduction during the overall treatment. The potential toxicity was further estimated by hematology and histopathology examination (Fig. 9, Fig. S30†). The hematological parameters of AST, ALT, BUN and CRE lacked any evidence of systemic toxicity. Besides, no remarkable pathological changes were found in the H&E staining of the liver, spleen, lung and kidney. However, noticeable myocardial necrosis was observed in the heart from mice treated with free DOX, and the plasma levels of LDH were simultaneously increased. All of the above experimental results demonstrated that RGD-sNPs can serve as a cancer nanomedicine with improved therapeutic efficacy and reduced side effects.

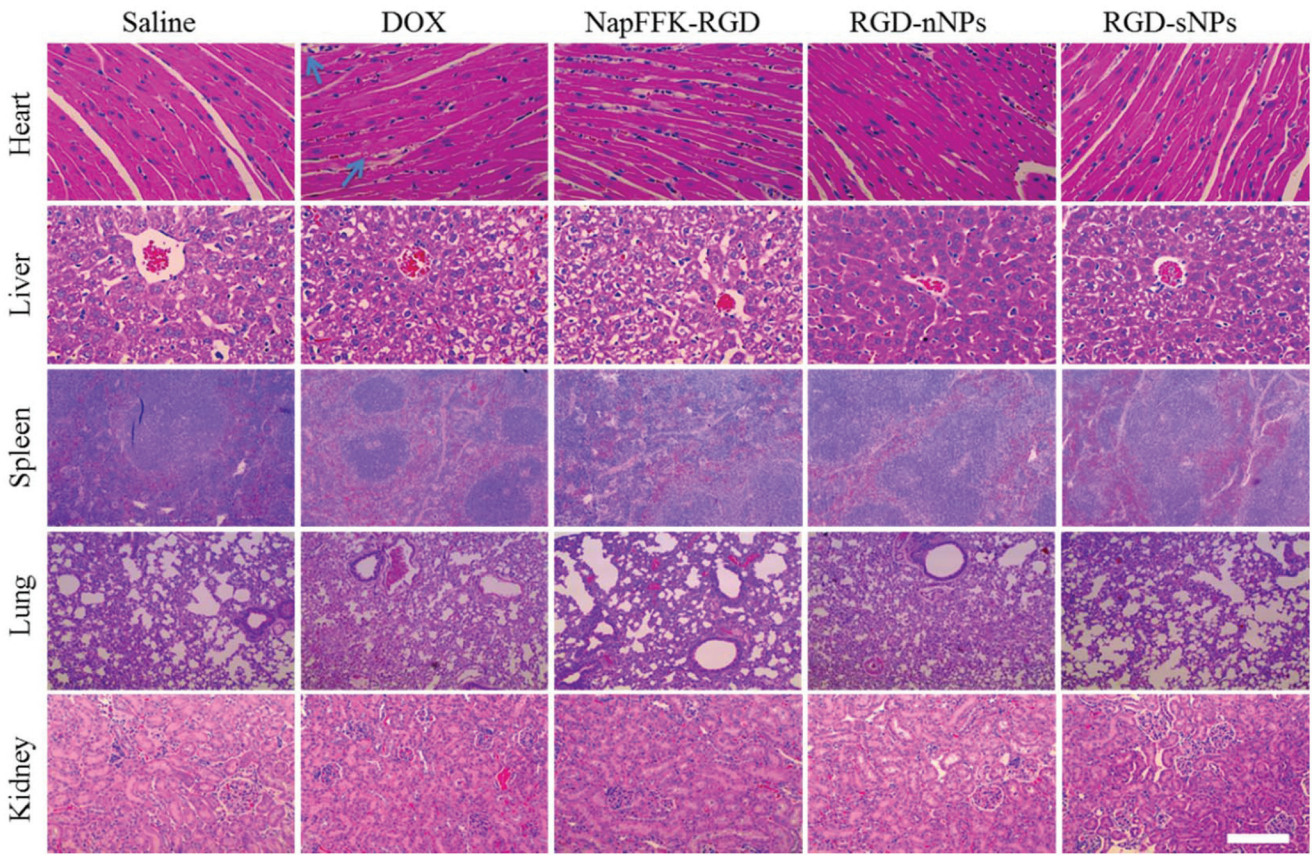

Fig. 9 The images of H&E staining for the heart, liver, spleen, lung and kidney resected from H22 tumor-bearing mice (blue arrows indicate myocardial necrosis, scale bar for 100 μm).

4. Conclusions

In summary, we developed a pH/MMP9 dual-sensitive sequentially responsive and continuously structure-transformable nanoparticle assembled from a doxorubicin-conjugated peptide with a comprehensively improved 'CAPIR cascade' for eventually enhancing therapeutic efficacy. The prodrug can self-assemble into spheroidal nanoparticles (RGD-sNPs) in a neutral environment with a particle size of 45.7 ± 5.4 nm and a slightly negative charge of −8.44 ± 1.4 mV. By a combination of passive and active targeting mechanisms, RGD-sNPs achieved considerable accumulation in the tumor site. The gathered nanoparticles would be transformed into nanofibers with a suitable diameter and length due to overexpressed MMP9 in the tumor microenvironment, resulting in deep tissue penetration, prolonged retention time and enhanced cellular uptake. Under weakly acidic conditions, the pH-sensitive hydrazone bond was cleaved accompanied by rapid DOX release for the subsequent induction of cytotoxicity and apoptosis, and by the formation of cytotoxic fibers for a synergistic antitumor effect. Therefore, RGD-sNPs showed a superior antitumor effect and a notably enhanced survival time of H22 tumor-bearing mice (a MMP9 high expression tumor model). The compromised antitumor efficacy of RGD-sNPs in the 4T1 orthotopic tumor model also revealed that it is very necessary to confirm the stimuli level in tumors (such as MMP9, MMP2, GSH, pH or ROS) when applying this kind of stimuli-responsive drug release or structure-transformable nanosystem in cancer therapy.

Conflicts of interest

The authors declare no competing financial interest.

Acknowledgements

This work was supported by the National Natural Science Foundation of China (81673374 and 81373360) and the Fundamental Research Funds for the Central Universities (2015ZDTD048 and 2018KFYYXJJ019). The authors thank the Analytical and Testing Center of Huazhong University of Science and Technology (HUST) for ^{1}H-NMR, HRMS, and CD measurements. The authors thank the Wuhan Institute of Virology Academia Sinica for TEM detection and the School of Basic Medicine, Tongji Medical College of HUST for confocal laser scanning microscopy experiments.

References

1 J. Shi, A. R. Votruba, O. C. Farokhzad and R. Langer, *Nano Lett.*, 2010, **10**, 3223–3230.
2 B. Aslan, B. Ozpolat, A. K. Sood and G. Lopez-Berestein, *J. Drug Targeting*, 2013, **21**, 904–913.
3 Q. Sun, Z. Zhou, N. Qiu and Y. Shen, *Adv. Mater.*, 2017, **29**, 1606628.
4 D. L. Stirland, J. W. Nichols, S. Miura and Y. H. Bae, *J. Controlled Release*, 2013, **72**, 1045–1064.
5 R. M. Rifkin, S. A. Gregory, A. Mohrbacher and M. A. Hussein, *Cancer*, 2006, **106**, 848–858.
6 H. Cabral and K. Kataoka, *J. Controlled Release*, 2014, **190**, 465–476.
7 F. Yuan, M. Leunig, S. Huang, D. A. Berk, D. Papahadjopoulos and R. K. Jain, *Cancer Res.*, 1994, **54**, 3352–3356.
8 A. A. Manzoor, L. H. Lindner, C. D. Landon, J.-Y. Park, A. J. Simnick, M. R. Dreher, S. Das, G. Hanna, W. Park and A. Chilkoti, *Cancer Res.*, 2012, **72**, 5566–5575.
9 W. Sun, T. Jiang, Y. Lu, M. Reiff, R. Mo and Z. Gu, *J. Am. Chem. Soc.*, 2014, **136**, 14722–14725.
10 L. Brannon-Peppas and J. O. Blanchette, *Adv. Drug Delivery Rev.*, 2012, **64**, 206–212.
11 J. B. Wolinsky, Y. L. Colson and M. W. Grinstaff, *J. Controlled Release*, 2012, **159**, 14–26.
12 P. Yang, Q. Luo, G. Qi, Y.-J. Gao, B. Li, J.-P. Zhang, L. Wang and H. Wang, *Adv. Mater.*, 2017, **29**, 1605869.
13 Y. Ji, Y. Xiao, J. He, C. Qian, W. Li, L. Wu, R. Chen, J. Wang, R. Hu, X. Zhang, Z. Gu and Z. Chen, *Adv. Sci.*, 2018, 1700867.
14 S. Guo, Y. Huang, Q. Jiang, Y. Sun, L. Deng, Z. Liang, Q. Du, J. Xing, Y. Zhao, P. Wang, A. Dong and X. Liang, *ACS Nano*, 2010, **4**, 5505–5511.
15 Q. H. Sun, M. Radosz and Y. Shen, *J. Controlled Release*, 2012, **164**, 156–169.
16 K. Cheng, Y. Ding, Y. Zhao, S. Ye, X. Zhao, Y. Zhang, T. Ji, H. Wu, B. Wang, G. J. Anderson, L. Ren and G. Nie, *Nano Lett.*, 2018, **18**, 3250–3258.
17 Y. Cai, H. Sheng, J. Zhan, M. Lin, L. Dai, C. Ren, Y. Shi, J. Liu, J. Gao and Z. Yang, *J. Am. Chem. Soc.*, 2017, **139**, 2876–2879.
18 H. M. Wang, Z. Feng and B. Xu, *Chem. Soc. Rev.*, 2017, **46**, 2421–2436.
19 T. Ji, Y. Zhao, Y. Ding, J. Wang, R. Zhao, J. Lang, H. Qin, X. Liu, J. Shi, N. Tao, Z. Qin, G. Nie and Y. Zhao, *Angew. Chem., Int. Ed.*, 2016, **55**, 1050–1055.
20 J. Li, Y. Kuang, J. Shi, J. Zhou, J. E. Medina, R. Zhou, D. Yuan, C. Yang, H. Wang, Z. Yang, D. M. Dinulescu and B. Xu, *Angew. Chem., Int. Ed.*, 2015, **54**, 13307–13311.
21 P. Zhang, A. G. Cheetham, Y. Lin and H. Cui, *ACS Nano*, 2013, **7**, 5965–5977.
22 J. Bhattacharyya, J. J. Bellucci, I. Weitzhandler, J. R. McDaniel, I. Spasojevic, X. Li, C.-C. Lin, J. T. A. Chi and A. Chilkoti, *Nat. Commun.*, 2015, **6**, 7939–7950.
23 S. Soukasene, D. J. Toft, T. J. Moyer, H. Lu, H. K. Lee, S. M. Standley, V. L. Cryns and S. I. Stupp, *ACS Nano*, 2011, **5**, 9113–9121.
24 V. P. Chauhan and R. K. Jain, *Nat. Mater.*, 2013, **12**, 958–12962.
25 B. R. Smith, P. Kempen, D. Bouley, A. Xu, Z. Liu, N. Melosh, H. J. Dai, R. Sinclair and S. S. Gambhir, *Nano Lett.*, 2012, **12**, 3369–3377.

26 K. Han, J. Zhang, W. Zhang, S. Wang, L. Xu, C. Zhang, X. Zhang and H. Han, *ACS Nano*, 2017, **11**, 3178–3188.
27 K. S. Chu, W. Hasan, S. Rawal, M. D. Walsh, E. M. Enlow, C. Luft, A. S. Bridges, L. J. Kuijer, M. E. Napier, W. C. Zamboni and J. M. DeSimone, *Nanomedicine*, 2013, **9**, 686–693.
28 J. H. Park, G. von Maltzahn, L. Zhang, M. P. Schwartz, E. Ruoslahti, S. N. Bhatia and M. J. Sailor, *Adv. Mater.*, 2008, **20**, 1630–1635.
29 Y. Liu, J. Du, M. Yan, M. Lau, J. Hu, H. Han, O. Yang, S. Liang, W. Wei, H. Wang, J. Li, X. Zhu, L. Shi, W. Chen, C. Ji and Y. Lu, *Nat. Nanotechnol.*, 2013, **8**, 187–192.
30 X. Hu, P. He, G. Qi, Y. Gao, Y. Lin, C. Yang, P. Yang, H. Hao, L. Wang and H. Wang, *ACS Nano*, 2017, **4**, 4086–4096.
31 S. Qiao, Y. Ma, Y. Wang, Y. Lin, H. An, L. Li and H. Wang, *ACS Nano*, 2017, **11**, 7301–7311.
32 P. Huang, Y. Gao, J. Lin, H. Hu, H. Liao, X. Yan, Y. Tang, A. Jin, J. Song, G. Niu, G. Zhang, F. Horkay and X. Chen, *ACS Nano*, 2015, **9**, 9517–9527.
33 L. Dong, Q. Miao, Z. Hai, Y. Yuan and G. Liang, *Anal. Chem.*, 2015, **87**, 6475–6478.
34 S. Zitzmann, V. Ehemann and M. Schwab, *Cancer Res.*, 2002, **62**, 5139–5143.
35 D. Kalafatovic, M. Nobis, J. Son, K. I. Anderson and R. V. Ulijn, *Biomaterials*, 2016, **98**, 192–202.
36 K. M. Tsoi, S. A. MacParland, X. Ma, V. N. Spetzler, J. Echeverri, B. Ouyang, S. M. Fadel, E. A. Sykes, N. Goldaracena, J. M. Kaths, J. B. Conneely, B. A. Alman, M. Selzner, M. A. Ostrowski, O. A. Adeyi, A. Zilman, I. D. McGilvray and W. C. Chan, *Nat. Mater.*, 2016, **15**, 1212–1221.
37 Y. Q. W. Wong, C. H. F. Yeo and W. H. Ang, *Angew. Chem., Int. Ed.*, 2014, **53**, 6752–6756.
38 C. Xu, Y. Ding, J. Ning, L. Yin, J. Zhou and J. Yao, *RSC Adv.*, 2016, **6**, 27542–27556.
39 C. Ju, R. Mo, J. Xue, L. Zhang, Z. Zhao, L. Xue, Q. Ping and C. Zhang, *Angew. Chem., Int. Ed.*, 2014, **53**, 6253–6258.
40 L. Wang, W. Li, J. Lu, Y.-X. Zhao, G. Fan, J.-P. Zhang and H. Wang, *J. Phys. Chem. C*, 2013, **117**, 26811–26820.
41 L. Wang, L.-L. Li, Y.-S. Fan and H. Wang, *Adv. Mater.*, 2013, **25**, 3888–3898.
42 C. Luo, J. Sun, D. Liu, B. Sun, L. Miao, S. Musetti, J. Li, X. Han, Y. Du, L. Li, L. Huang and Z. He, *Nano Lett.*, 2016, **16**, 5401–5408.
43 A. Xu, P. Yang, C. Yang, Y. Gao, X. Zhao, Q. Luo, X. Li, L. Li, L. Wang and H. Wang, *Nanoscale*, 2016, **8**, 14078–14083.
44 N. Panté and M. Kann, *Mol. Biol. Cell*, 2002, **13**, 425–434.
45 X. Guo, X. Wei, Y. Jing and S. Zhou, *Adv. Mater.*, 2015, **27**, 6450–6456.
46 Y. Kuang and B. Xu, *Angew. Chem., Int. Ed.*, 2013, **52**, 6944–6948.
47 Y. Gao, C. Berciu, Y. Kuang, J. Shi, D. Nicastro and B. Xu, *ACS Nano*, 2013, **7**, 9055–9063.
48 D. Zhang, G. Qi, Y. Zhao, S. Qiao, C. Yang and H. Wang, *Adv. Mater.*, 2015, **27**, 6125–6130.
49 M.-P. Chien, A. S. Carlini, D. Hu, C. V. Barback, A. M. Rush, D. J. Hall, G. Orr and N. C. Gianneschi, *J. Am. Chem. Soc.*, 2013, **135**, 18710–18713.
50 A. Tanaka, Y. Fukuoka, Y. Morimoto, T. Honjo, D. Koda, M. Goto and T. Maruyama, *J. Am. Chem. Soc.*, 2015, **137**, 770–775.
51 Y. Gao, Y. Kuang, Z.-F. Guo, Z. H. Guo, I. J. Krauss and B. Xu, *J. Am. Chem. Soc.*, 2009, **131**, 13576–13577. Q13
52 E. Blanco, H. Shen and M. Ferrari, *Nat. Biotechnol.*, 2015, **33**, 941–951.
53 O. C. Farokhzad and R. Langer, *ACS Nano*, 2009, **3**, 16–20.
54 D. Wang, Z. Xu, H. Yu, X. Chen, B. Feng, Z. Cui, B. Lin, Q. Yin, Z. Zhang, C. Chen, J. Wang, W. Zhang and Y. Li, *Biomaterials*, 2014, **35**, 8374–8384.
55 Hu. Du, C. Cui, L. Wang, H. Liu and G. Cui, *Mol. Pharm.*, 2011, **8**, 1224–1232.
56 C. F. X. Li, C. Dong, X. Zhang, X. Zhang and Y. Gao, *Drug Des., Dev. Ther.*, 2015, **9**, 4613–4620.
57 E. Veneti, R. S. Tu and D. T. Auguste, *Bioconjugate Chem.*, 2016, **27**, 1813–1821.